Computer-Aided Design 38 (2006) 342–366

COMPUTER-AIDED DESIGN

www.elsevier.com/locate/cad

Laplace–Beltrami spectra as ‘Shape-DNA’ of surfaces and solids

Martin Reuter, Franz-Erich Wolter *, Niklas Peinecke

Division of CG, University of Hannover, Welfenlab, D-30167 Hannover, Germany

Received 25 May 2005; accepted 31 October 2005

Abstract

This paper introduces a method to extract ‘Shape-DNA’, a numerical fingerprint or signature, of any 2d or 3d manifold (surface or solid) by taking the eigenvalues (i.e. the spectrum) of its Laplace–Beltrami operator. Employing the Laplace–Beltrami spectra (not the spectra of the mesh Laplacian) as fingerprints of surfaces and solids is a novel approach. Since the spectrum is an isometry invariant, it is independent of the object’s representation including parametrization and spatial position. Additionally, the eigenvalues can be normalized so that uniform scaling factors for the geometric objects can be obtained easily. Therefore, checking if two objects are isometric needs no prior alignment (registration/localization) of the objects but only a comparison of their spectra. In this paper, we describe the computation of the spectra and their comparison for objects represented by NURBS or other parametrized surfaces (possibly glued to each other), polygonal meshes as well as solid polyhedra. Exploiting the isometry invariance of the Laplace–Beltrami operator we succeed in computing eigenvalues for smoothly bounded objects without discretization errors caused by approximation of the boundary. Furthermore, we present two non-isometric but isospectral solids that cannot be distinguished by the spectra of their bodies and present evidence that the spectra of their boundary shells can tell them apart. Moreover, we show the rapid convergence of the heat trace series and demonstrate that it is computationally feasible to extract geometrical data such as the volume, the boundary length and even the Euler characteristic from the numerically calculated eigenvalues. This fact not only confirms the accuracy of our computed eigenvalues, but also underlines the geometrical importance of the spectrum. With the help of this Shape-DNA, it is possible to support copyright protection, database retrieval and quality assessment of digital data representing surfaces and solids.

A patent application based on ideas presented in this paper is pending.

Keywords: Laplace–Beltrami operator; Shape invariants; Fingerprints; Shape matching; Database retrieval; Copyright protection; NURBS; Parameterized surfaces and solids; Polygonal meshes

1. Introduction

The characterization and design of the shape of 3d-objects are central problems in computer graphics and geometric modeling. The development of software and hardware tools to design and visualize the shape of 3d-objects has advanced rapidly during the past twenty years. Nonetheless, fundamental problems pertaining to the characterization of shape are still widely unresolved. It is, for example, a basic question to quickly identify and retrieve a given object stored in a huge database or to find all similarly shaped objects. During the past forty years, a vast number of shape matching and searching techniques have been developed (e.g. using moments, spherical harmonics or Reeb graphs—a recent survey can be found in Iyer et al. [39], see also [30]). It should be pointed out that most approaches dealing with shape matching describe procedures to realign the geometric objects, usually called localization or registration (cf. [53,60]), and work only on a specific representation (mainly polygonal meshes) of the object. Other techniques describe subdivision or decomposition of an object into smaller features (e.g. [9] or [37]) that are then compared in a second step.

The point-set of a solid 3d-object with smooth boundary may be described in very different ways (cf. [65]), for example in boundary representation (B-Rep) using NURBS surface patches. This may cause difficulties to decide if two objects have the same or different shapes. Even when restricted to NURBS surfaces, it is not easy to decide if the given objects are similar in their shape. A simple comparison of the control points used to represent the boundary surfaces does not help at all, because identical patches can be represented with different control points. Both patches first need to be represented with

* Corresponding author.

E-mail addresses: reuter@gdv.uni-hannover.de (M. Reuter), few@gdv.uni hannover.de (F.-E. Wolter), peinecke@gdv.uni-hannover.de (N. Peinecke).

0010-4485//$ - see front matter © 2005 Elsevier Ltd. All rights reserved.
doi:10.1016/j.cad.2005.10.011

the same basis functions implying equal knot vectors and equal degrees of the employed NURBS basis functions. The problem becomes even more complicated if we consider the possibility that the solid's boundary surfaces might be represented in various other ways, e.g. by trigonometric functions, by implicitly defined functions or by polygonal meshes (planar polygonal faces), that have to be compared with each other.

In some of these cases, the problem of identifying shapes (for example, to protect the copyright of the designer) has been approached with the help of watermarks. For this purpose, visible or invisible watermark information is embedded into the representation or geometry of an object. Later on, this information can be retrieved and the object can be identified. This is of special interest when dealing with delicate high precision material, e.g. turbine blades, whose design needs major research effort and expensive investments. Even though NURBS patches are very popular today, most watermark techniques deal with polygonal meshes only. Often the watermark data is embedded into these meshes by slightly modifying the vertex location, the connectivity of the mesh or the frequency domain employing mesh-spectral analysis (cf. [6,49]). For NURBS surfaces watermarking is more difficult and only very few algorithms exist. An algorithm proposed by Ohbuchi et al. [48] does not change the surface, but is not very robust. Generally, watermarks can be destroyed by a representation change or by a reparametrization of the object, if they are not embedded into the geometry. On the other hand, embedding data into the geometry rather than into the representation changes the shape of the object which is unacceptable in many cases. It should be noted that the watermarking technique is limited to the comparison of watermark information, which in general is not related to the shape. Therefore, it cannot be used for shape matching but only for the identification of previously marked objects.

A superior identification method avoiding both problems of watermarking (i.e. geometry changes or representation dependency) is to identify the shape of an object by geometric invariants that we will call *fingerprints* or *signatures*. An example for a fingerprint of shape intrinsic information to identify shape via registration/alignment of umbilics can be found in [42] or [43]. However, our approach is different because we use sets of geometric invariants that are sufficiently complete to identify isometric objects so we can avoid realignment procedures as a safeguard for tests of identical shape. Of course, fingerprint techniques cannot distinguish between several copies of the same object, since they only depend on the shape. In such a case, watermarks have to be applied in order to discriminate identical copies. Nevertheless, an advantage of the use of shape related fingerprints is that shape can be compared indirectly through the fingerprints (especially if similar shapes lead to similar fingerprints). In addition to shape identification, the fingerprint technique can therefore be used for shape matching.

Shape intrinsic information does not depend on the given representation of the shape and can be understood as a fingerprint of the shape (if enough information is contained). Many geometric shape invariants (e.g. circumference, surface area, volume, bounding sphere or eigenvalues of the inertia tensor) have strong limitations with respect to the amount of completeness up to which these invariants determine the shape of an object. Therefore, we propose the following properties that optimally should be fulfilled by a shape fingerprint (e.g. a vector of numbers/shape invariants associated with the given object):

1. [ISOMETRY]: Congruent solids (or isometric surfaces) should have the same fingerprint independently of the object's given representation and location. Therefore, the fingerprint should be an isometry invariant.
2. [SCALING]: For some applications, it is necessary that the fingerprint is independent of the object's size, therefore the fingerprint should optionally be scaling invariant.
3. [SIMILARITY]: Similarly, shaped solids should have similar fingerprints. The fingerprint should depend continuously on shape deformations.
4. [EFFICIENCY]: The effort needed to compute those fingerprints should be reasonable.
5. [COMPLETENESS]: Ideally, those fingerprints should give a complete characterization of the shape, thus representing the shape uniquely. One step further it would be desirable that those fingerprints could be used to reconstruct the solid.
6. [COMPRESSION]: In addition it would also be desirable that the fingerprint data should not be redundant, i.e. a part of it could not be computed from the rest of the data.
7. [PHYSICALITY]: Furthermore, it would be nice if an intuitive geometric or physical interpretation of the meaning of the fingerprints would be available.

Concerning property [ISOMETRY] let us give the following definitions:

Definition 1 (*Isometry*)
Two geometric objects are *isometric* if a homeomorphism from one to the other exists preserving (geodesic) distances, i.e. mapping curves to curves with equal arc length. This homeomorphism is then called an *isometry*.

Definition 2 (*Congruency*)
Two geometric objects are *congruent* if they can be transformed into each other by rigid motions (translations and rotations) as well as reflections.

It should be noted that isometric planar domains in 2d and isometric solids in 3d Euclidean space are already uniquely determined in their respective space up to rigid motions and reflections. For planar shapes and 3d-solids congruency and isometry are the same. Surfaces on the other hand that are bend or folded without stretching (without changing the metric) stay isometric even though they are not congruent. The property [ISOMETRY] (and of course [SIMILARITY]) is important in situations where near isometric surfaces like hands with different finger positions or faces with different expressions are to be compared and identified. See, e.g. [27] for a method using discrete geodesic distances and multidimensional scaling to generate similar signature surfaces (that still need to be aligned for final comparison), and see [14] for an application to face recognition. An isometry invariant fingerprint is often desired in shape matching, since it depends

- *only* on the (intrinsic) shape, independent of any representation;
- *not* on the actual embedding and is therefore independent of the spatial position and isometric deformation of the object.

Very often invariants are used to classify objects. For example in knot theory, a branch of topology, knot invariants (e.g. the Alexander polynomial or the more recent Jones and the Homfly polynomials) are used to distinguish knotted space curves (cf. [1]). For surfaces there exist, for example, topological invariants (cf. [57]) such as homotopy invariants including, e.g. homotopy groups and homology groups or the well-known Euler characteristic. Another important topological invariant of a manifold is its orientability (being a non-homotopic invariant, because the non-orientable Moebius strip and the orientable cylinder have the circle as deformation retract and are therefore homotopic to it). Although all these topological shape invariants are interesting and useful, they cannot distinguish any two homeomorphic objects such as two 3d-solids, e.g. obtained by deforming a topological full 3d-disk.

There exist theoretical invariants determining the isometry type of a surface or solid completely up to isometry. Indeed, the first fundamental tensor (defined independently of a parametrization) is a complete isometry invariant [25]. However, this invariant can generally not be used to check if two given parametrizations represent isometric manifolds. In order to compare this invariant for two objects, they first have to be parametrized on a common parameter space. These parametrizations have to be constructed in a way that they map the same point in parameter space to the two corresponding points on each manifold. This task is as difficult as finding the isometry itself, which generally is a very difficult problem. The first fundamental tensor can be used to check if a diffeomorphism is an isometry. But even this task is difficult, as it requires checking every point.

A manifold can theoretically be determined completely up to translation and rotation by the first and the second fundamental tensor [25]. Like before, those two tensors do not provide an easy tool to check if two distinct parametrizations refer to congruent manifolds. The medial axis transform (MAT) (defined uniquely for a solid body) provides a shape invariant that is a complete shape descriptor (cf. reconstruction theorem [64–66]). Using the MAT for testing the congruence of two given 3d-solids would also require checking if the respective medial axis sets (usually collections of surface patches) are congruent, a task that again is not easy at all in general. Therefore, all shape invariants listed above cannot be used efficiently to detect if two distinct geometrical object representations refer to congruent or isometric objects. We think that this paper offers a remedy for the aforementioned difficulties occurring in shape comparison problems. This holds because the shape invariants presented in this paper can be used efficiently for shape comparison (once they have been computed).

This paper proposes to use the sequence of eigenvalues (spectrum) of the Laplace operator of a planar domain or 3d-solid or the Laplace–Beltrami operator of a surface or parametrized solid in Euclidean space as a fingerprint. The Laplace operator can be seen as the special case of the Laplace–Beltrami operator with a Euclidean metric. These Laplace operators are linear differential operators defined on a corresponding vector space of differentiable functions, the latter being defined on a domain in Euclidean space or on a Riemannian manifold, respectively. Those differentiable functions are supposed to be zero on the boundary of the surface or of the domain in case the boundary is not empty (Dirichlet boundary condition). The Neumann boundary condition forces their derivatives in the normal direction of the boundary curve to be a fixed function or to be constantly zero. The Laplace operators assign the trace of their Hessian to the latter functions (defined on the domain or on the surface). In the surface case, the Hessian must be defined invariantly of the surface parametrization using only the Riemannian metric of the surface.

This fingerprint (i.e. the eigenvalues) can be calculated for different object representations in different dimensions and can even be calculated for grayscale or color images. We consider a gray scale image as a surface defined by the graph of a height function being the gray scale intensity function of the image. The color image can, e.g. be understood as a surface (two-manifold) in a five-dimensional Euclidean space whose coordinates include the intensity parameters of the red, green, blue values assigned to any (x, y) pixel of the image. It is possible as well to understand other even higher dimensional signals as height functions and therefore as manifolds, whose Laplace–Beltrami spectra can be computed. Another advantage of this method is that it can even be applied to solids containing cavities (solids bounded by several not connected surfaces), for example, an ice-cube containing fully enclosed bubbles. Most techniques only working on boundary representations, not on the solid itself, have difficulties with several boundary components. With our method, one can compare the 2d boundary as well as the 3d volume for two given solids.

The fingerprint presented here fulfills the desired properties above (with the only exception of [COMPLETENESS]). Since the eigenvalues are isometry invariants, this fingerprint is independent of the objects representation (especially its parametrization), its spatial position and, as we will see later, even of the object's size [SCALING] (if desired). This isometry invariance makes registration or localization of the objects completely unnecessary. The isometry invariance is very restrictive compared to the topological invariance. As mentioned before, isometry even determines the congruence of objects in important cases such as planar shapes or 3d-solids. In other words, if limited to these very common solid objects, their shapes are uniquely determined by their isometry class. The fingerprint proposed here consists of a family of non-negative numbers (the eigenvalues) that can be compared easily and fast, permitting this approach to be used in time-critical applications such as database retrieval. Because the spectrum of the Laplace–Beltrami operator contains intrinsic shape information we call it 'Shape-DNA'. We will show that this Shape-DNA can be used (like DNA-tests) to identify objects in practical applications. As in real life, the DNA does not completely characterize a subject. As we will discuss later identical twins exist with different shape but exactly the same Shape-DNA. Even though these twins are shaped differently they still have quite a few common geometric properties (exactly those properties that are determined by the spectrum). It should be noted that in real life human fingerprints (determined by phenotype) can distinguish identical twins, while DNA-tests (genotype) cannot. Therefore, we think that Shape-DNA is the more appropriate term. Beyond the identification of shapes, the Shape-DNA can even be used to detect similarities.

A special name for the Laplace–Beltrami spectra is even helpful to distinguish it from other spectra. To avoid any misunderstanding, note that the continuous Laplace–Beltrami operator does not operate on any mesh vertices, but rather on the underlying manifold itself. It is therefore different from discrete Laplacians on graphs or meshes. Even though these discrete Laplacians have been used for, e.g. dimensionality reduction [5] or mesh compression [41], the introduction of our computation of the Laplace–Beltrami spectra of the underlying manifolds in the areas of geometric modeling—CAD in particular and in computer graphics in general—is completely new. The only exceptions are our recent proceedings publication [56] outlining briefly some of the ideas and results presented in this paper and [65] containing a sketchy description of some basic ideas and goals. More details and background can be found in [55]. Moreover, the application of the Laplace–Beltrami spectra as Shape-DNA in order to discriminate and search for objects in geometric databases is new (cf. our german patent application [67]). Although a considerable amount of theoretical research has been done in geometry on the Laplace–Beltrami operator, very little work dealing with computational research exists (see e.g. Huntebrinker [38] for a numerical computation of the Laplace–Beltrami spectrum on 3d hyperbolic spaces).

One of the reasons why the spectra of the continuous Laplace and especially the Laplace–Beltrami operator have not yet been considered in the area of geometric modeling and computer graphics is that their computation is not easy at all, with respect to the theoretical effort (employing Riemannian geometry), and somewhat cumbersome with respect to the numerical effort involved. However, with the recent and continuing advancement of hardware development, the computations needed to determine surface spectra (e.g. the first 1000 or more eigenvalues) of the Laplace–Beltrami operator have become conveniently feasible even on a fairly modest personal computer. This shows that the requested [EFFICIENCY] can be achieved as well. Improvements concerning the efficient computation of the spectrum are also foreseeable.

We shall present this paper in a self-contained way such that it should be accessible to a researcher in geometric modeling who is not an expert on the tools from partial differential equations and differential geometry used here. Therefore, we will review some concepts from analysis and elements from differential geometry used for the Laplace–Beltrami operator and its properties (Section 2). We also need some concepts from numerical analysis on finite element methods used to compute solutions for partial differential equations (Section 3) and describe some techniques (like meshing) needed for the actual implementation (Section 4). Then we present a method to numerically extract geometric data from the eigenvalues (Section 5) and show how the Shape-DNA can be used to identify shapes and detect similarities for use in innovative applications (Section 6).

2. Theoretical background

In this section we will explain the theoretical background that is needed to understand the spectrum of the Laplace operator and its computation.

Let f be a real-valued function, with $f \in C^2$, defined on a Riemannian manifold M (differentiable manifold with Riemannian metric, cf. Berger [7]). With another function g defined like f we define the Nabla operator ∇ (that will be needed later for the variational formulation) and the Laplace–Beltrami operator Δ to be

$$\nabla(f,g) := \langle \operatorname{grad} f, \operatorname{grad} g \rangle \qquad \Delta f := \operatorname{div}(\operatorname{grad} f) \tag{1}$$

with $\langle\, , \rangle$ being the scalar product, grad f the gradient of f and div the divergence on the manifold [17].

The Nabla operator and the Laplace–Beltrami operator are linear differential operators. They can be calculated in local coordinates. Given a local parametrization

$$\psi : \mathbb{R}^n \to \mathbb{R}^{n+k} \tag{2}$$

of a submanifold M of $\mathbb{R}^{n+k}$ with

$$g_{ij} := \langle \partial_i \psi, \partial_j \psi \rangle, \qquad G := (g_{ij}), \qquad W := \sqrt{\det G}, \\ (g^{ij}) := G^{-1}. \tag{3}$$

(where $i, j=1,\ldots,n$ and det denotes the determinant), we get:

$$\nabla(f,g) = \sum_{i,j} g^{ij}\partial_i f \partial_j g \qquad \text{and}$$

$$\Delta f = \frac{1}{W}\sum_{i,j}\partial_i(g^{ij}W\partial_j f) \tag{4}$$

If M is a domain in the Euclidean plane $M\subset\mathbb{R}^2$, the Laplace–Beltrami operator reduces to the well-known Laplacian:

$$\Delta f = \frac{\partial^2 f}{(\partial x)^2} + \frac{\partial^2 f}{(\partial y)^2} \tag{5}$$

The Helmholtz equation (also known as the Laplacian eigenvalue problem) is stated as

$$\Delta f = -\lambda f. \tag{6}$$

The solutions of this equation represent the spatial part of the solutions of the wave equation. In the surface case $f(u, v)$ in Eq. (6) can be understood as the natural vibration form (also eigenfunction) of a homogeneous membrane with the eigenvalue λ. The solutions of the general vibration problem are the solutions $f(u, v)$ of this differential equation on the surface. Any constants of the material are ignored. The standard boundary condition of a fixed membrane is $f\equiv 0$ on the boundary of the surface domain (Dirichlet boundary condition) (see Fig. 1 for two eigenfunctions of the disk). Because of this physical interpretation, the question whether the eigenvalues of the Laplace operator determine the shape of a planar domain, has been rephrased by the late mathematician L. Bers in a terse, impressively concise and pictorial way: ‘Can one hear the shape of a drum?’ (cf. Protter [54] for a historic account). Another important boundary condition (namely the Neumann condition) does not force the function to a given value on the boundary but rather forces its derivative in the normal direction of the boundary curve to a fixed function (often to zero). Since the boundary of a membrane can therefore vibrate freely this condition is sometimes called natural boundary condition (instead of forced or essential as for the Dirichlet condition). The advantage of the Neumann condition is that a small hole in the surface (e.g. a missing triangle) does not change the spectrum as much as in the case of the Dirichlet condition. For manifolds without boundary, the spectrum is of course equal to the spectrum with Dirichlet boundary condition.

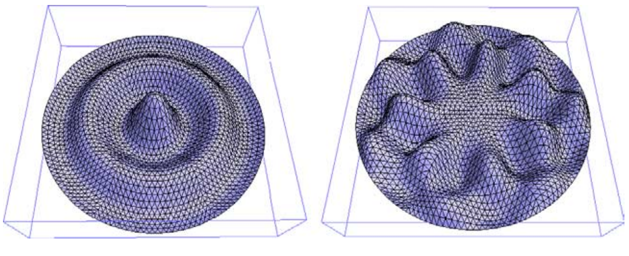

Fig. 1. Eigenfunction 30 and 50 of the disk.

2.1. Properties of the spectrum

The following paragraphs will describe well-known results on the Laplace–Beltrami operator.

- The spectrum is defined to be the family of eigenvalues of the Helmholtz equation (Eq. (6)), consisting of a diverging sequence $0\leq\lambda_1\leq\lambda_2\leq\cdots\uparrow+\infty$, with each eigenvalue repeated according to its multiplicity and with each associated finite dimensional eigenspace [8, p. 142]. In the case of a closed manifold without a boundary, the first eigenvalue λ_1 is always equal to zero, because in this case the constant functions are non-trivial solutions of the Helmholtz equation. If a Dirichlet boundary exists, the first eigenvalue is always greater than zero, since the only constant solution is trivial (because of the boundary condition). Generally, the first eigenvalue is always simple and the corresponding eigenfunction has no nodal lines (zero sets of the function). The nodal lines of the nth eigenfunction subdivide the domain into maximal n subdomains [20]. In case only the Neumann boundary condition is used, the first eigenvalue will always be zero with all constant eigenfunctions.
- The spectrum is an isometric invariant as it only depends on the gradient and divergence which in turn are defined to be dependent only on the Riemannian structure of the manifold (Eq. (4)). This implies property [ISOMETRY].
- Furthermore, we know that scaling a n-dimensional manifold by the factor a results in scaled eigenvalues by the factor $1/a^2$. Therefore, by normalizing the eigenvalues, shape can be compared regardless of the object’s scale (property [SCALING]). This fact can be proved quite easily for any dimension n.

Let M be a compact n-dimensional Riemannian manifold of class C^∞ with the local parametrization $h:\mathbb{R}^n\to\mathbb{R}^{n+k}$. The scaled manifold with the parametrization $\bar{h}:=ah$ possesses the partial derivatives

$$\partial_k\bar{h} = a\partial_k h \quad (k=1,\ldots,n) \quad \text{implying } \bar{g}^{ij} = \frac{1}{a^2}g^{ij} \quad \text{and}$$

$$\bar{W} = a^2 W,$$

using the notation defined in Eq. (3).

With u being a solution to

$$\Delta_h u = \frac{1}{W}\sum_{i,j}\partial_i(g^{ij}W\,\partial_j u) = -\lambda u$$

we have found u as a solution to

$$\Delta_{\bar{h}} u = \bar{W}^{-1}\sum_{i,j}\partial_i(\bar{g}^{ij}\bar{W}\,\partial_j u) = \frac{1}{a^2 W}\sum_{i,j}\partial_i(g^{ij}W\,\partial_j u) = -\frac{1}{a^2}\lambda u.$$

- The spectrum depends continuously on the shape of the membrane [20], thus complying with property [SIMILARITY]. Moreover, it can be shown with similar arguments that the spectrum depends continuously on the Riemannian metric of the manifold in general.

- The numerical computation of the spectrum as described later in Section 3 can already be done with a standard personal computer, therefore the requested [EFFICIENCY] can be satisfied as well.
- The property [COMPLETENESS] is not fulfilled by the spectrum, because some non-isometric manifolds with the same spectrum exist (see Section 2.2 for more details).
- The question if a sequence of n real numbers ($S=\{a_1=0<a_2\leq a_3\leq\cdots\leq a_n\}$) can be the beginning of the spectrum of a compact Riemannian manifold X has been discussed by Colin de Verdière [19]. It is shown that for any such finite sequence S, there always exists a compact Riemannian manifold X with $\dim(X)\geq 3$ always exists realizing S as the beginning of its Laplace spectrum. This result also means that given any positive integer n, a Riemannian manifold exists, such that the multiplicity of the first non-zero eigenvalue is n. In the case of a closed Riemannian surface ($\dim(X)=2$), there are bounds to the multiplicities depending linearly on the genus. However, in the case of a surface, the result by Colin de Verdière holds also for finite sequences of the form $S=\{a_1=0<a_2<a_3<\cdots<a_n\}$. These results are interesting in the context of property [COMPRESSION]. We can now prove Assertion 1.

Assertion 1 (*Mutual independency of eigenvalues*) An arbitrary eigenvalue λ_k of a compact Riemannian manifold (M, g) cannot be computed from a finite number of other eigenvalues of (M, g) in general (i.e. if the manifold is unknown). Precisely, it is not possible to find a function $h(S)$ (called redundancy function) depending on a finite subsequence S of the eigenvalues $\lambda_1\cdots\lambda_n$, that computes a special eigenvalue $\lambda_k\notin S$ so that for all compact Riemannian manifolds containing S in their spectra, λ_k is also contained in their spectra (at the same position k). We will prove this indirectly.

Proof. Let $h(S)$ be a redundancy function as stated above computing a $\lambda_k\notin S$. If we construct the smallest sequence S_0 of values containing λ_k as well as S then S_0 is still finite. We can violate the redundancy $h(S)$ by replacing λ_k with a different value and call this new sequence S_1. Because S_1 violates the redundancy h (that was valid for all manifolds containing S in their spectra), it cannot be the beginning of a valid spectrum, so no compact Riemannian manifold (M, g) with S_1 as the beginning sequence of its spectrum can exist. This yields a contradiction to the result of Colin de Verdière, since a manifold exists for any finite beginning sequence of its spectrum. □

Another interesting (but weaker) result following directly from Assertion 1 can be stated.

Corollary 1 (*Impossibility of finite characterization*)
No subsequence S of a spectrum Spec(M) of any unknown compact Riemannian manifold M already determines the whole spectrum.

Proof. Since no redundancy function $h(S)$ computing just a single eigenvalue λ_k can be found (see Assertion 1), it is of course impossible to find a function $h(S)$ computing several eigenvalues (or even the whole spectrum). □

Of course, classes of manifolds exist (like the disks or the rectangle) where one or two eigenvalues already determine the size and the shape and therefore the whole spectrum. In other words, if we know we have a rectangle, we need just two eigenvalues to find its side lengths. Corollary 1 states that without prior knowledge of the manifold, a characterization is impossible by a finite subsequence of the spectrum. Therefore, the spectrum cannot be compressed into a finite subsequence (see property [COMPRESSION]) without losing information. As we will discuss later, the whole spectrum on the other hand determines the shape of some manifolds (e.g. balls in any dimension among solids, cf. Remark 1).

- A substantial amount of geometrical and topological information is known to be contained in the spectrum (see Section 2.3), therefore the property [PHYSICALITY] is fulfilled. Even though we cannot crop a spectrum without losing information, we will show that it is possible to extract important information just from the first few eigenvalues (approx. 500).

2.2. Isospectrality

Unfortunately, the spectrum does not completely determine the shape of the underlying manifold, even though geometrical data is contained in the eigenvalues. Manifolds with identical spectra will be called isospectral manifolds. The question formulated by L. Bers and first published by Kac in 1966 (see [40]), asking if the shape of a planar region is determined by the spectrum of the Laplacian, has been answered negatively. Originally, the question was stated by Gel'fand in a more general and theoretical context concerning arbitrary manifolds (see [32]). After many years of research in 1992, it could be shown (cf. [34]) that pairs of isospectral but not congruent planar domains exist. Meanwhile, various pairs of planar (and also non-planar) non-isometric but isospectral manifolds are known. Fig. 2 shows two isospectral planar domains found by Buser et al. [16]. One can show these domains to be isospectral by using the technique of transplanting the eigenfunctions of one domain to the other.

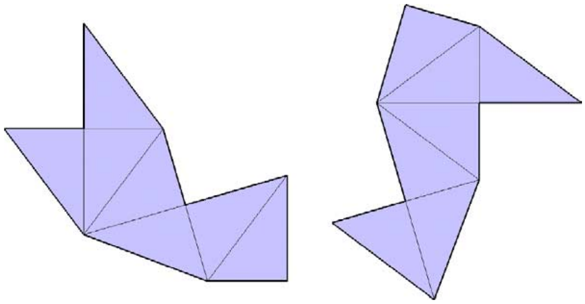

Fig. 2. Isospectral planar domains.

Therefore, it will not be possible to satisfy property [COMPLETENESS]. Nevertheless, no three pairwise isospectral but non-isometric manifolds have been constructed so far and all known pairs of isospectral planar domains have been shown to be non-convex with non-smooth boundaries. The only examples of pairs of convex domains in Euclidean space, being isospectral but not congruent, were found in four or higher dimensional spaces [33]. It is not sure if triples or isospectral continuous deformations exist in lower dimensions at all. The constructed examples (i.e. pairs of isospectral domains) were always somewhat artificial and appear to be exceptional. Furthermore, some shapes can be characterized completely by their spectrum (e.g. simple analytic surfaces of revolution among their type, cf. Zelditch [69] or the *n*-dimensional disks among solids, cf. Kac [40] for planar disks and see Remark 1 in Section 6.1. for higher dimensions). Therefore, there is some hope that isospectrality of non-isometric manifolds (at least in lower dimensions up to 3) is a relatively rare phenomenon. For instance, Osgood et al. [52] showed that isospectral families of metrics on a given surface are compact in a natural C^∞ topology. Furthermore, for the special case of Riemann surfaces (namely surfaces with constant negative curvature), Buser [15] was able to derive an upper bound for the number of isospectral but non-isometric surfaces depending only on the genus. For all of these reasons and also based on experimental studies, we feel that the spectra of the Laplace–Beltrami operator have significant discrimination power, strong enough to be used in contemporary applications.

In this context, it should be noted that there is evidence that in the case of a fixed graph, the unknown weight function can be reconstructed by knowledge of the discrete spectrum of the graph. This graph spectrum can be obtained by the discrete analogue of the Laplacian, the Laplace–Kirchhoff operator (cf. [36]). The weight reconstruction is still an area of active research. For the 'reverse' case of a given weight function (satisfying special conditions), the unknown graph structure can be reconstructed by knowledge of the spectrum of the Laplace–Kirchhoff operator (see Halbeisen and Hungerbühler [36]).

2.3. Geometric information

A substantial amount of geometric and topological information is known to be contained in the spectrum. These results endorse property [PHYSICALITY]. Beyond that, they even contribute towards the desired property [COMPLETENESS] considering that all geometrical and topological properties determined by the spectrum have to be identical for isospectral objects. In this section we will present an overview on known results. Finally, we state our Theorem 4 that ensures the rapid convergence of the 'heat trace' and thus the possibility to actually compute geometric and topological information with only the first few eigenvalues of an object.

In response to the question 'can one hear the shape of a drum?', it is possible to 'hear' the following information:

(1) It has been shown that if two compact Riemannian manifolds M and $\bar{M}$ are isospectral, then $\dim M = \dim \bar{M}$ and (Riemannian) volume(M) = volume$(\bar{M})$ [8, p. 215]. Hence, the spectrum determines the dimension and the volume of a Riemannian manifold. McKean and Singer [44] showed the equality of the respective curvature integrals for the scalar curvature K (i.e. the Gauss curvature in case of a surface) for isospectral manifolds $\left(\int_M k = \int_{\bar{M}} \bar{K}\right)$.

(2) In the case of a compact d-dimensional manifold M with compact $(d-1)$-dimensional boundary B in addition to the results in (1), the (Riemannian) volume of the boundary B can be 'heard' [44]. However, in order to obtain the curvature integral of M and the integrated mean curvature $\int_B J$ the spectrum of the double of M is generally needed.

(3) In the cases of a closed surface (dim = 2) and of a planar domain with a smooth boundary, McKean and Singer [44] deduced the possibility to 'hear' the Euler characteristic from the spectrum. Thus, Kac's conjecture [40] of hearing the number of holes in the case of a planar region M with smooth boundary B can be obtained. For surfaces with smooth boundary, the Euler characteristic and the geodesic curvature integral of the boundary curve can be obtained from spectral data as well, if one additionally employs the spectrum of the surface double.

Remark. On a surface (dim(M) = 2), the Riemannian volume of M is the surface area and the Riemannian volume of the boundary is its length.

We will now give a short overview on the background needed to understand the connection between the eigenvalues and the geometric data mentioned above [in (1)–(3)]. More details can be found in Berger [7], and in [22]. Everything started with the following result by Weyl [62] for the two-dimensional [63] for the three-dimensional case for a planar domain with boundary (cf. also [7] or [17]).

Theorem 1 (*Weyl—Asymptotic growth of eigenvalues*)
If D is a bounded region of $\mathbb{R}^d$ with piecewise smooth boundary B and if $0 < \lambda_1 \le \lambda_2 \cdots$ is the spectrum and $N(\lambda)$ the number of eigenvalues $\le \lambda$, counted with multiplicity, then

$$N(\lambda) \sim \frac{\omega_{\mathrm{d}} \mathrm{vol}(D) \lambda^{d/2}}{(2\pi)^d} \tag{7}$$

as $\lambda \to +\infty$, where vol(D) *is the volume of D and*

$$\omega_{\mathrm{d}} := \frac{\pi^{d/2}}{\Gamma\left(\frac{d}{2}+1\right)} \tag{8}$$

is the volume of the unit disk in $\mathbb{R}^d$. In particular,

$$\lambda_n \sim 4\pi^2 \left(\frac{n}{\omega_{\mathrm{d}} \mathrm{vol}(D)}\right)^{2/d} \quad as\, n \uparrow \infty \tag{9}$$

especially,

$$\lambda_n \sim \frac{4\pi}{\mathrm{vol}(D)} n \ \ for\, d = 2, \qquad and$$

$$\lambda_n \sim \left(\frac{6\pi^2}{\mathrm{vol}(D)}\right)^{2/3} n^{2/3} \ \ for\, d = 3. \tag{10}$$

Minakshisundaram and Pleijel [46] extended this result and showed more generally that for a closed Riemannian manifold, $N(\lambda)$ has also an asymptotic approximation whose first term is determined by the volume of the manifold and its dimension. Not much later the heat kernel, the fundamental solution of the heat equation, was constructed by Minakshisundaram [45] and the asymptotic expansion of the heat trace was inspected. We will give a short explanation of these concepts, as they are the basis of our computations.

Let M be a Riemannian manifold. The heat equation is given by

$$\frac{\partial u}{\partial t} + \Delta_2(u) = 0, \quad u : [0,\infty) \times M \to \mathbb{R}, \tag{11}$$

with Δ_2 being the Laplace–Beltrami operator with respect to the second variable (i.e. the space variable x). Here, $u(t, x)$ is the temperature at the point $x \in M$ at time t. Given an initial temperature distribution $u(0, x) = f(x)$ and a Dirichlet boundary condition ($u(t, x) \equiv 0$ for x on the boundary of M) then a fundamental solution of the heat equation on M (also called heat kernel) is a function $K{:}(0,\infty) \times M \times M \to M$, satisfying:

(1) $K(t, x, y)$ is C^1 in t and C^2 in x and y.
(2) K solves the heat equation: $(\partial K/\partial t) + \Delta_2(K) = 0$.
(3) K fulfills the boundary condition: $K(t, x, y) = 0$ if x is on the boundary of M, and
(4) $\lim_{t \to 0^+} \int_M K(t,x,y) f(y) \mathrm{d}V(y) = f(x)$ uniformly for every function f that is continuous on M and vanishes on the boundary of M.

A solution of the heat equation (11) can be obtained with the heat kernel by adding the contribution of each point to the initial data:

$$u(t,x) = \int_M K(t,x,y) f(y) \mathrm{d}V(y). \tag{12}$$

For Theorem 2, refer to Chavel [17, p. 139 and 169].

Theorem 2 (*Sturm–Liouville decomposition*)
Let (M, g) *be an n-dimensional compact Riemannian manifold, with eigenvalues* (*counted with multiplicities*) λ_n $(n \geq 1)$ *and associated orthonormal real eigenfunctions* ξ_n. *A unique heat kernel* $K(t, x, y)$ *exists on* (M, g). *The heat kernel can be expressed as*

$$K(t,x,y) = \sum_{n=1}^{\infty} \mathrm{e}^{-\lambda_n t} \xi_n(x) \xi_n(y) \tag{13}$$

with absolute and uniform convergence for each $t > 0$. *The heat trace of the Dirichlet Laplacian* Δ *on a Riemannian manifold* M *is defined by*

$$Z(t) := \int_M K(t,x,x) \mathrm{d}V(x) \tag{14}$$

and can thus be expressed by

$$Z(t) = \sum_{n=1}^{\infty} \mathrm{e}^{-\lambda_n t} \int_M (\xi_i(x))^2 \mathrm{d}V(x) = \sum_{n=1}^{\infty} \mathrm{e}^{-\lambda_n t} \tag{15}$$

Z(t) is sometimes called the partition function of (M, g).

Theorem 3 (*Asymptotic heat trace expansion*)
The heat trace has the following asymptotic expansion when $(t \to 0^+)$, (cf. [45,54] *for an overview*):

$$Z(t) = (4\pi t)^{\frac{-\dim(M)}{2}} \left(\sum_{i=0}^{n} c_i t^{\frac{i}{2}} + \mathrm{o}(t^{\frac{n+1}{2}}) \right) \tag{16}$$

With one of the Landau symbols, **O**:

$$f(t) = 0(g(t)) :\Leftrightarrow \exists\, k \in \mathbf{R} : \left| \frac{f(t)}{g(t)} \right| < k \text{ when } (t \to 0). \tag{17}$$

c_0 *of the asymptotic expansion Z(t) is the volume of the manifold, but even more geometric information can be extracted as shown by McKean and Singer* [44] *who obtained the first three coefficients in the case of smooth compact d-dimensional Riemannian manifolds M with or without compact* $(d-1)$*-dimensional boundary B*

$$c_0 = \mathrm{vol}(M), \quad c_1 = -\frac{\sqrt{\pi}}{2} \mathrm{area}(B), \quad \text{and}$$
$$c_2 = \frac{1}{3} \int_M K - \frac{1}{6} \int_B J \tag{18}$$

with the scalar curvature K and the mean curvature J at the boundary. Therefore, for a planar region with a smooth boundary B the number of holes $h < \infty$ *can be obtained*

$$c_2 = \frac{2\pi}{3}(1 - h) \tag{19}$$

and for closed two-dimensional manifolds the Euler characteristic E:

$$c_2 = \frac{2\pi}{3} E \tag{20}$$

These results confirm the earlier results by Weyl and Kac for planar regions, namely that the area and the length of the boundary curve can be extracted (see above). Further coefficients of the asymptotic expansion above have been calculated (see Protter [54]).

Weyl's law (Eq. (9)) can be described as a result of Theorem 3 (using Karamata's Tauberian theorem and writing

$$\sum_n \mathrm{e}^{-\lambda_n t} = \int_0^{\infty} \mathrm{e}^{-\lambda_n t} \, \mathrm{d}N(\lambda) \text{ cf.}$$

[28, p. 446, theo. 4]). It is therefore valid for Riemannian manifolds in general. Using Weyl's law we will now discuss how fast the series defining $Z(t_0)$ in Eq. (15) converges for a fixed t_0. We derive the subsequent result (that we could not find in the literature).

Theorem 4 (*Rapid convergence of heat trace series*) *The remainder term* $R_{n_0}(t)=Z(t)-Z_{n_0}(t)$ *of the* n_0*th partial sum*

$$Z_{n_0}(t):=\sum_{n=1}^{n_0}\mathrm{e}^{-\lambda_n t} \tag{21}$$

describing the heat trace $Z(t)$ *vanishes very fast*:

$$R_{n_0}(t)<\frac{n_0^{1-k_1 t}}{k_1 t-1}=:R_1(t) \quad \text{when } t>\frac{1}{k_1} \tag{22}$$

Here k_1 is a constant depending on the geometry of the domain and on n_0. In the special case of a two-dimensional manifold, the remainder is bounded from above by

$$R_{n_0}(t)<\frac{\mathrm{e}^{-(n_0+1)k_0 t}}{1-\mathrm{e}^{-k_0 t}}=:R_0(t) \tag{23}$$

with a constant k_0 depending on the geometry of the domain and on n_0.

Proof. We can write Weyl's law (Eq. (9)) as

$$\lambda_n \sim 4\pi^2\left(\frac{n}{\omega_{\mathrm{d}}\mathrm{vol}(D)}\right)^{2/d}=an^{2/d} \quad \text{as } n\uparrow\infty \tag{24}$$

with the substitution $a:=4\pi^2(\omega_{\mathrm{d}}\mathrm{vol}(D))^{-2/d}$ (only depending on the dimension d of M). This asymptotic relationship means that

$$\begin{aligned}\lambda_n \sim an^{2/d} &\Leftrightarrow \lim_{n\to\infty}\frac{\lambda_n}{an^{(2/d)}}=1\\ &\Leftrightarrow \forall\varepsilon>0\,\exists\, n_0:\left|\frac{\lambda_n}{an^{(2/d)}}-1\right|\le\varepsilon \quad (\forall n\ge n_0)\\ &\Leftrightarrow \left|\lambda_n-an^{(2/d)}\right|\le\varepsilon\, an^{(2/d)} \quad (\forall n\ge n_0)\end{aligned} \tag{25}$$

If $\lambda_n\le an^{2/d}$ it follows that

$$\lambda_n\ge(1-\varepsilon)an^{2/d} \tag{26}$$

In the other case ($\lambda_n\ge an^{(2/d)}$), Eq. (26) holds trivially when choosing $0<\varepsilon<1$. Therefore, we can write

$$\lambda_n>k_0 n^{2/d} \tag{27}$$

and because exponential decay is much faster than polynomial we get

$$\lambda_n>k_1\ln n \tag{28}$$

in general (for all λ_n with $n>n_0$ and n_0 depending on the constant).

We can now find an upper bound for the remainder term $R_{n_0}(t)$ for a fixed t using Eq. (28):

$$\begin{aligned}R_{n_0}(t)&=\sum_{n=n_0+1}^{\infty}\mathrm{e}^{-t\lambda_n}<\sum_{n=n_0+1}^{\infty}\mathrm{e}^{-k_1 t\ln n}\\ &=\sum_{n=n_0+1}^{\infty}n^{-k_1 t}<\int_{n_0}^{\infty}x^{-k_1 t}\mathrm{d}x=\frac{1}{k_1 t-1}n_0^{1-k_1 t}\end{aligned} \tag{29}$$

if $k_1 t>1$.

This term vanishes very rapidly. The condition $k_1 t>1$ can be fulfilled for small t by choosing n_0 large enough to get a sufficiently large k_1.

Of course the real convergence of $Z(t)$ is even faster, since the term above is just a rough upper bound. A tighter upper bound to the remainder term can be given in the case of a surface ($d=2$) with Eq. (27), because the series describing $Z(t_0)$ converges as rapidly as the geometric series:

$$\begin{aligned}R_{n_0}(t)&=\sum_{n=n_0+1}^{\infty}\mathrm{e}^{-t\lambda_n}<\sum_{n=n_0+1}^{\infty}\mathrm{e}^{-k_0 tn}=\sum_{n=n_0+1}^{\infty}(\mathrm{e}^{-k_0 t})^n\\ &=\frac{\mathrm{e}^{-(n_0+1)k_0 t}}{1-\mathrm{e}^{-k_0 t}}\end{aligned} \tag{30}$$

□

Our observations above regarding the rapid convergence of the series describing $Z(t_0)$ imply that there is hope to obtain a decent approximation of the first coefficients c_i in Eq. (16) using a moderate number of eigenvalues that can be determined by feasible numerical computations.

3. Numerical computation

In this section we will explain the numerical computation of the eigenvalues of surfaces and solids with the help of finite elements. Readers familiar with the finite element method may simply skip this section.

3.1. Variational problem

For the numerical computation (next section), the first step is to translate the Laplacian eigenvalue problem into a variational problem. To accomplish this, we use Greens formula

$$\int\!\!\int\varphi\,\Delta f\,\mathrm{d}\sigma=-\int\!\!\int\nabla(f,\varphi)\mathrm{d}\sigma \tag{31}$$

with $\varphi\equiv 0$ on the boundary [11, p. 227] and the Nabla operator

$$\nabla(f,\varphi)=\sum g^{ij}\partial_i f\,\partial_j\varphi \tag{32}$$

We multiply the Helmholtz equation with test functions $\varphi\in C^2$ ($\varphi\equiv 0$ on the boundary). Integrating over the area and using Greens formula we obtain

$$\begin{aligned}&\int\!\!\int\varphi\,\Delta f\,\mathrm{d}\sigma=-\lambda\int\!\!\int\varphi f\,\mathrm{d}\sigma\\ &\Leftrightarrow\int\!\!\int\sum g^{ij}\partial_i f\,\partial_j\varphi\,\mathrm{d}\sigma=\lambda\int\!\!\int\varphi f\,\mathrm{d}\sigma\end{aligned} \tag{33}$$

with $\mathrm{d}\sigma=W\,\mathrm{d}u\,\mathrm{d}v$ being the surface element in the surface case. Every function $f\in C^2$ on the open domain and continuous on the boundary solving the variational equation for all test functions φ is a solution to the Laplace eigenvalue problem [13, p. 35].

3.2. Discretization

For the numerical computation of the eigenvalues and eigenfunctions, a discretization of the problem is necessary. The solution of the variational problem in the surface case is approximated using the Galerkin technique as follows (see, e.g. Strang [58]):

- Firstly we choose n linearly independent form functions: $F_1(\vec{x}),\dots,F_n(\vec{x})$ defined on the parameter space.
- Secondly we use these functions as a basis of a vector space and allow the following linear combination as approximation of the solution:

$$f(\vec{x}) \approx F(\vec{x}) := U_1 F_1(\vec{x}) + \cdots + U_n F_n(\vec{x}).$$

- Finally we calculate the n unknown coefficients $U_i \in \mathbb{R}$ by substituting f in the variational equation and by choosing n different test functions φ_i to get n equations. In order to keep the problem symmetric we choose the test functions to be the n-form functions.

As form functions for the Finite Element Method, we used linear, quadratic and cubic polynomials defined on triangular elements in the parameter space of the surface or on tetrahedral elements in case of a solid. The higher degree functions lead to a better approximation and consequently to better results. Employing Eq. (33) then with the two symmetric matrices

$$A = (a_{lm}) := \left(\int\!\!\int \left(\sum_{j,k} (\partial_j F_l)(\partial_k F_m) g^{jk} \mathrm{d}\sigma \right) \right)$$
$$B = (b_{lm}) := \left(\int\!\!\int F_l F_m \mathrm{d}\sigma \right) \tag{34}$$

the variational equation can be written as the general eigenvalue problem:

$$AU = \lambda BU \tag{35}$$

Here U is the vector $(U_1,\dots,U_n)$ and A, B are sparse positive (semi-) definite symmetric matrices since all eigenvalues are greater or equal to zero. The solution vectors U (eigenfunctions) with corresponding eigenvalues λ can then be calculated.

It should be noted that the integrals mentioned above are computed on the surface (not on vertices of a given mesh) and therefore independent of the given mesh (as long as the mesh fulfills some refinement and condition standards). Beyond that, this method is completely independent of the given parametrization.

4. Implementation

In the present state we can use the following object representations as input: A triangulation of a 2d-parameter space together with any given parametrized surface as input (our sample computations include NURBS, faceted surfaces, etc.). Furthermore, polyhedra or tetrahedrized 3d-parameter spaces can be used as input. As we will see later, it is possible to glue parameter spaces to each other or to themselves in order to construct closed or more complex objects.

Different techniques are used for mesh generation. The triangulation of the parameter space employs a Delaunay triangulation technique, resulting in triangles whose smallest angles are maximized [51]. Furthermore, a surface sensitive triangulation technique based on Chen and Bishop [18] has been implemented for the creation of high quality meshes on surfaces. This method uses surface curvature and circumellipses (instead of circumcircles) in the parameter space to control the surface mesh quality and density (see Fig. 3).

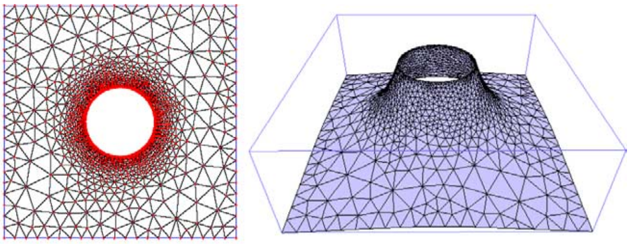

Fig. 3. Surface sensitive meshing.

In order to be independent of the given resolution, it is possible to further refine a triangulation or tetrahedrization. Since we are interested in many eigenvalues and eigenfunctions at once and since we do not know beforehand where a dense mesh is needed for a specific eigenfunction, it is wise to refine the mesh globally. It is also possible to refine locally. This makes sense, for example, in areas with concavities or with high surface curvature, since most eigenfunctions will need fine meshes in these areas. Furthermore, for local refinement an a posteriori error estimate can be used to improve the calculation of a specific eigenfunction. For example, the error estimate of Zienkiewicz-Zhu (see Ainsworth and Oden [2]) detects regions where the approximation of an eigenfunction yields errors. These regions can then be refined locally to improve the results in a second computation.

Often the global refinement of a given triangulation is done by dividing every edge into halves, thus creating four smaller triangles within each triangle, each of them similar to their parent. Further refinement can be achieved by repeating this step. The problem with this method is that the total number of triangles t raises exponentially with the steps n of refinement ($t=4^n t_{\text{old}}$) (with t_{old} triangles in the initial mesh). After only a few steps the mesh is too large for efficient FEM computations. It is therefore helpful to have a refinement method that provides more densely spaced refinement steps. In this way the maximal possible number of triangles can be approached without exceeding it to early.

In order to be able to generate more closely spaced levels of global refinement, the simple approach from above can be modified slightly. Every edge can be divided into n equidistant segments (see Fig. 4). This way, it is possible to generate n^2 similar smaller triangles in just a single step. Since only this

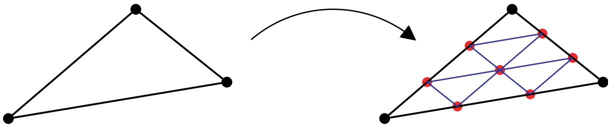

Fig. 4. Triangle refined with edge trisection.

single refinement step will be used, the total number of finer triangles t yields a polynomial growth ($t = n^2 t_{\text{old}}$).

Even though this method seems to be very simple, it is quite tricky to implement. The creation of a huge amount of triangles in a single step makes bookkeeping very complicated. Many new neighborhood relations have to be generated and the uniqueness of every new vertex has to be assured. This turns out to be challenging especially with vertices and neighborhood relations at the edges of each parent triangle. The new neighbor-triangles might not yet exist (the neighbor parent might not have been visited yet). In order to avoid revisiting triangles later, the triangle indices of the future neighbors have to be pre-calculated. Nevertheless, all of this can be done within a single run through the triangle list, resulting in a very time efficient and flexible routine for global refinement.

To be able to glue different patches to each other or even glue a patch to itself we developed a special data structure called 'structural atlas'. The structural atlas consists of one or several polygonal triangulated parameter spaces, associated parametrizations (functions mapping a point of the parameter space into $\mathbb{R}^3$) and a list of edge pairs glued to each other. The glued edges must lie on the boundaries of the parameter spaces. With the help of this data structure, it is possible to use a broad variety of parametrizations to construct surfaces, since the boundary of the parameter space does not necessarily need to be the boundary of the surface patch anymore. The atlas can easily be employed to construct a torus, a sphere and many other closed or non-closed surfaces. It is not necessary that pairs of glued edges are mapped to identical positions, therefore even objects like flat tori that cannot be embedded in $\mathbb{R}^3$ can be constructed. This is a great advantage since models with correct topology (e.g. boundary representations where the patches are glued correctly to each other) but with gaps or holes in the geometry can be given as input without any pre-processing.

Fig. 5 shows the construction of a cylinder with spherical caps. The cylinder with spherical caps consists of three parameter spaces glued to each other with corresponding parametrizations mapping the triangles to hemispheres and the rectangle to the cylinder shell. The reason why it is possible to glue different patches to each other is simply that different local parametrizations do not change the values of the integrals used to compute the two matrices A and B, defined invariantly only employing the Riemannian metric. Therefore, our method also works with faceted surfaces (such as the boundary of 3d-polyhedra).

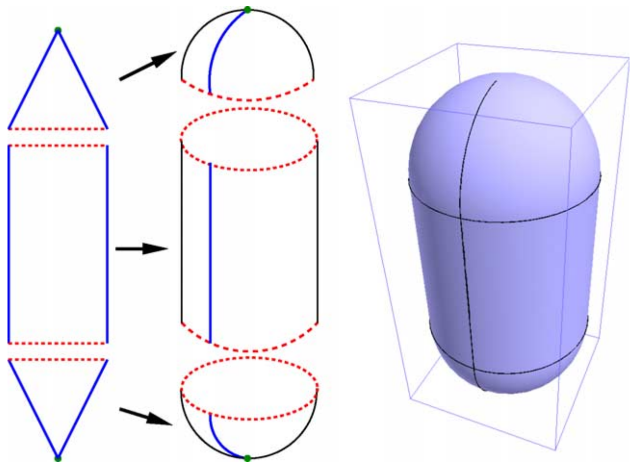

Fig. 5. Glued parameter spaces of a cylinder with spherical caps.

Finally, before computing the surface integrals mentioned earlier, the Cuthill algorithm [23] is applied to the interior vertices of the triangulation or tetrahedrization to keep the usage of memory small. By renumbering the vertices in a way that adjacent vertices get numbers close to each other, the bandwidth of the two resulting sparse symmetric matrices can be reduced. These band matrices can be stored very efficiently. Because of the boundary condition ($f \equiv 0$ on the boundary), the vertices on the boundary do not need to be indexed. After calculating the integrals (being the entries of the two matrices), a NAG (Numerical Algorithms Group) FORTRAN library [47] is used to solve the general eigenvalue problem. In addition to the eigenvalues, it is possible to compute the eigenfunction in the same manner. If only a small number of eigenvalues is needed, a Lanczos algorithm [35] can be employed to solve large symmetric eigenvalue problems even faster than this is possible with the direct method used in the NAG library.

4.1. Convergence and accuracy

It is well known that the convergence rate of the FEM method with degree p behaves asymptotically (with an error of order $O(h^{p+1})$) as the element size h tends to zero and if the exact solution contains no singularities (see, e.g. Zienkiewicz and Taylor [70]). Given two approximate solutions, u_1 obtained with mesh size h and u_2 with mesh size $h/2$, then a close approximation of the exact solution u can be calculated from

$$\left(\frac{O(h^{p+1})}{O(h^{p+1}/2^{p+1})}\right) \approx \frac{u_1 - u}{u_2 - u} \approx 2^{p+1} \tag{36}$$

in most practical cases [70]. This is possible because the described convergence rate is generally reached very fast. It should be noted that many discrete Laplace–Beltrami operators defined on meshes and used for computer graphics applications are not convergent in general, some of them are not even an approximation of the continuous case (cf. Xu [68]). Furthermore, most of these discrete operators are only discretizations of the Laplacian in the case of manifolds without boundary.

In addition to the known convergence rate, further possibilities exist to assess our results. Our FEM computation yields very accurate results as can be verified when comparing the approximated results with the exact ones known from theory in some cases (rectangle, circle, sphere, cube, ball, cylinder, etc.). Additionally, the fact that we are able to extract the correct geometrical data (volume, boundary length, Euler characteristic) from the heat trace expansion indicates that the calculated eigenvalues are very precise.

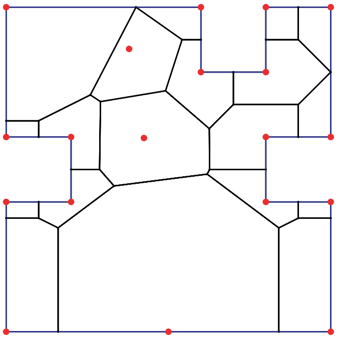

Fig. 6. Subdomains of polygon.

4.2. Planar polygonal domains

For planar polygonal domains, there exists a method for calculating the eigenvalues of the Laplacian that uses the knowledge of the correct solution at the singularities (the vertex points of the polygon) employing radial basis functions in polar coordinates and the integration of Fourier–Bessel functions on subdomains. This method was proposed by Descloux and Tolley [24] and improved by Driscoll [26] and yields very exact results (proven in [10]). To be able to use their method for any planar polygonal domain, we had to extend it to handle inner domains. We also developed and implemented a fully automatic algorithm to subdivide any polygon into subdomains (see Fig. 6 for an example). The star shaped subdomains around each center need to obey special conditions dictated by Descloux and Tolleys method. For example, the size of each subdomain is bounded by the distance of its center to the closest neighbor center. With our software, it is possible to find a close approximation to an eigenvalue inside a specified interval. It is therefore efficiently possible to calculate a few eigenvalues very exactly. For larger quantities of eigenvalues (e.g. 100 or even 1000), this method is not suitable, though it might be possible to combine it with our FEM computation to improve our pre-calculated results.

Note that Descloux and Tolley [24] were already inspired by the method of particular solutions that had been proposed by Fox et al. [29]. This method has been revived by Betcke and Trefethen [10] quite recently. They were able to overcome its numerical limitations by forcing the solutions to be largely non-zero in the interior of the planar domain. With their refined method they computed highly accurate eigenvalues and verified their correctness.

5. Extraction of geometric data

5.1. Error computation and extrapolation

The numerical extraction of geometric data from the heat trace (cf. Eqs. (15) and (16)) appears to be completely new. The asymptotic expansion (16) as $(t\to 0^+)$ can be understood as

$$X(t) := (4\pi t)^{\dim(M)/2} Z(t) = \sum_{i=0}^{n} c_i t^{i/2} + \mathrm{O}(t^{(n+1)/2}) \tag{37}$$

With the substitution $x := \sqrt{t}$ and $d := \dim(M)$ we get

$$X(x) = (4\pi)^{d/2} \sum_{i=1}^{\infty} x^d \,\mathrm{e}^{-\lambda_i x^2} = \sum_{i=0}^{n} c_i x^i + \mathrm{O}(x^{n+1}) \tag{38}$$

and for $(x\to 0^+)$ the first coefficient c_0 can be calculated:

$$\lim_{x\to 0} X(x) = \lim_{x\to 0}\left(\sum_{i=0}^{n} c_i x^i + \mathrm{O}(x^{n+1})\right) = c_0 \tag{39}$$

The coefficients c_1 and c_2 can be calculated similarly using the limit values of the derivatives

$$c_1 = \lim_{x\to 0} X'(x) = \lim_{x\to 0} (4\pi)^{d/2} \sum_{i=1}^{\infty} x^{d-1}(d - 2\lambda_i x^2)\mathrm{e}^{-\lambda_i x^2}$$
$$c_2 = \frac{1}{2}\lim_{x\to 0} X''(x) \tag{40}$$

The only handicap is that instead of the whole spectrum only the first n eigenvalues λ_i are known. Therefore, the infinite sum in $X(x)$ can only be evaluated partially for the first n summands. However, as we showed in Theorem 4, we receive good results for sufficiently large x because the convergence rate is fast enough for x large enough. Of course, the function

$$X_n(x) := (4\pi)^{d/2} \sum_{i=1}^{n} x^d \,\mathrm{e}^{-\lambda_i x^2} \tag{41}$$

and its derivatives yield a large error if x gets too small, since the infinite sum is replaced by a finite summation. Therefore, the values c_i have to be computed by extrapolation. Actually, the error stays quite small for larger x and then increases rapidly if x drops below a certain value. In Figs. 8 and 9 (that we will discuss in more detail later), the function $X_{1000}(x)$ is plotted with the first 1000 known eigenvalues of the sphere. It can be seen that $X(x)$ breaks away when x gets smaller than 0.1. The interesting question, which values of $X(x)$ are reliable and which are not, can now be answered with the help of Theorem 4 via computation of the constants $k_0(1000)$ and $k_1(1000)$.

We can see in Fig. 7, where the first 5000 eigenvalues of the sphere are plotted (step function $S(n)$), that we can get a safe approximation of $k_1 = 143$ since the linear growth of the

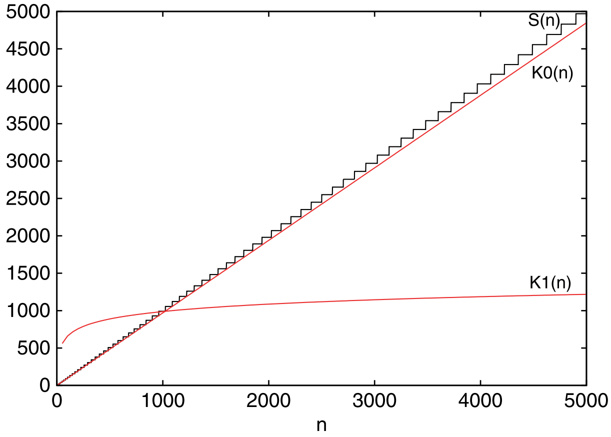

Fig. 7. Spectrum of the sphere with lower bounds.

eigenvalues larger than λ_{1000} will stay above the logarithmic function $K_1(n):=143\ln n$ (cf. Theorem 4). Since we have a two-dimensional problem (sphere surface) and therefore a linear growth of the eigenvalues, a tighter lower bound for the eigenvalues can be given by the line $K_0(n):=k_0 n$ with $k_0=0.96969$ (again see Fig. 7). Of course, in general, one cannot be sure that all higher eigenvalues will stay above the bounds $\lambda_n > K_{0,1}(n)$. This theoretical objection can be diminished since the eigenvalues usually start to obey Weyl's law very early and since many more eigenvalues are computed than needed for X_n, which can be used to verify and if necessary to correct the constant. To be on the safe side, one can simply apply the weaker logarithmic bound K_1 and use the constant k_1 for the error estimation.

Using the constants k_0 and k_1, the upper bound of the error (remainder term $R_0(x)$ and $R_1(x)$, respectively) can be computed via Theorem 4. In Figs. 8 and 9 the function $X_{1000}(x)$ is plotted together with the upper bounds of its remainder term. In the first case we computed the general bound R_1 using k_1 that holds in any dimension. As shown in Assertion 1, this bound can only be applied for $x > \sqrt{(1/k_1)} \approx 0.08363$ which is still sufficiently small. It can be seen that the values of $X(x)$ for $x > 0.1$ are very good. Using the constant k_0 (that can be applied since the sphere is a two-dimensional manifold) yields a much better upper bound R_0 of the error (see Fig. 9). We observe that values for $x > 0.08$ are already very good. These left bounds (x-values where the function $R(x)$ shrinks below a given error ϵ) can be computed numerically and depend on the number of eigenvalues used.

In Fig. 10 we see these left bounds (x-values) plotted against the used number of eigenvalues n (again in the case of the sphere) for a given $\epsilon=0.0000001$. This graph shows, how far we can approach zero given a number of eigenvalues (with an error certain to stay below ϵ). As can be seen, the graph shrinks rapidly at the beginning, it then slows down at around 500 eigenvalues and decreases only slightly above 1000 eigenvalues. In other words, it does not help much to use more than 1000 eigenvalues for the computation, since the left bound barely keeps moving. The inverse plot $n(x)$ is also interesting, because it shows how many eigenvalues are actually needed if $X(x)$ shall be computed with an error below ϵ for a given x.

Since we cannot approach zero any closer than the left bound $x(n)$, the computation of the limits of X and its derivatives for $x\to 0$ in Eqs. (39) and (40) have to be done via extrapolation. For this purpose, we constructed an interpolating rational function (using the NAG library) and evaluated the interpolant at $x=0$. This automatic process yields very good results when computing the first coefficient c_0. Because the derivatives of the interpolant are not as precise, we interpolated the derivatives of $X(x)$ successively instead. Since no error bounds have been constructed for the derivatives so far, some user interaction was necessary for the appropriate placement of the sampling points. We are currently working on improved methods using different extrapolation functions employing also the known derivatives at some sample points. We think that with more suitable extrapolation or fitting routines and a refined error analysis for the derivative values (X' and X'') further automation and a higher accuracy of the computed geometric data will be possible.

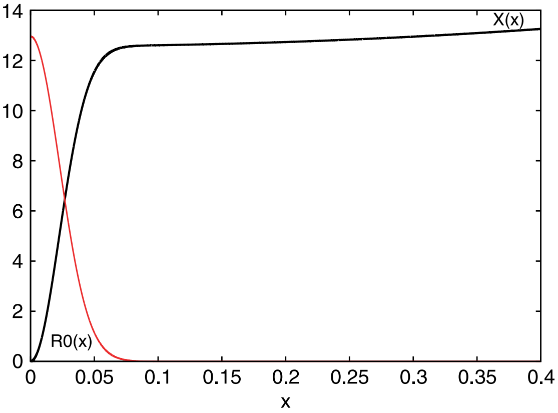

Fig. 9. $X(x)$ for the sphere with error using k_0.

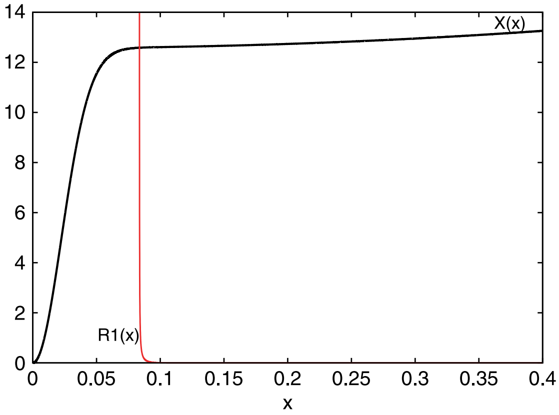

Fig. 8. $X(x)$ for the sphere with error using k_1.

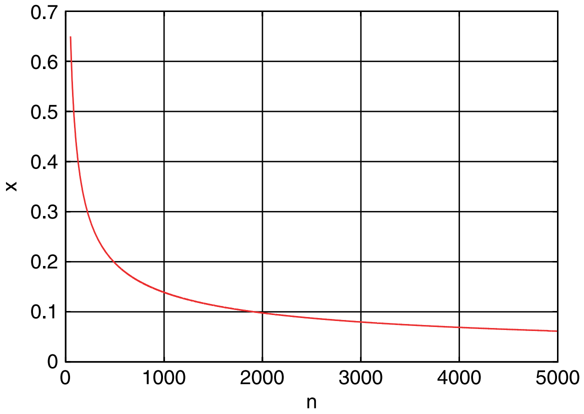

Fig. 10. Left bounds $x(n)$ with $\epsilon=0.0000001$.

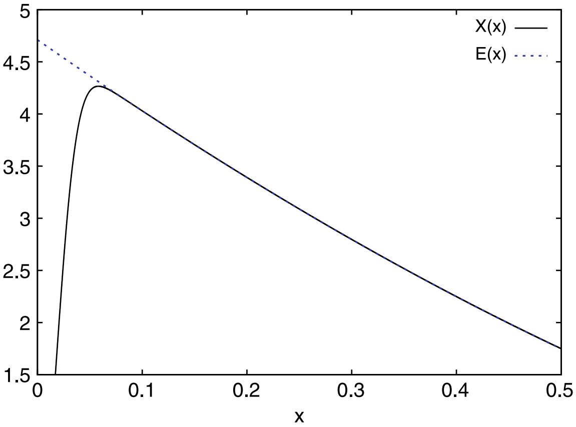

Fig. 11. Extrapolation of $X_{500}(x)$ for the ellipse.

5.2. Examples

5.2.1. Ellipse

In the case of the ellipse with radii ($r_1=1.0$, $r_2=1.5$), we used an affine transformation of the disk for the numerical eigenvalue computation (cf. Section 6.1 and Fig. 13 for a parametrization), keeping the mesh well conditioned. In Fig. 11 the function $X_{500}(x)$ is plotted together with its extrapolating rational function $E(x)$. The computed value $A=E(0)=c_0=4.71075$ describes the area of the ellipse, a number quite close to the real area $1.5\pi\approx 4.712389$. A different polynomial extrapolation function

$$A_p := E_p(x) = 4.71121 - 7.04364x + 0.19791x^2 \tag{42}$$

looks exactly the same, but yields an even better approximation of the area

$$E_p(0) = c_0 \approx 4.71121. \tag{43}$$

The approximated boundary length

$$L \approx \frac{-2}{\sqrt{\pi}} c_1 \approx \frac{-2}{\sqrt{\pi}}(-7.02176) \approx 7.9232 \tag{44}$$

which is close to the real length 7.93272 (computed by integration of the boundary curve) could be obtained by extrapolating the first derivative $X'(x)$. Furthermore, the number of holes h, a topological invariant and determining the Euler characteristic

$$h = \frac{-3c_2}{2\pi} + 1 \approx \frac{-3\times 2.0862}{2\pi} + 1 \approx 0.00391 \approx 0 \tag{45}$$

could be obtained correctly (of course, the result has to be an integer value). All the results with relative error can be found in Table 1.

Table 1
Geometric data of ellipse

	Real	Extracted	Error (%)
A	4.712389	4.71075	0.035
A_p	4.712389	4.71121	0.025
L	7.93272	7.9232	0.12
h	0	0.00391	–

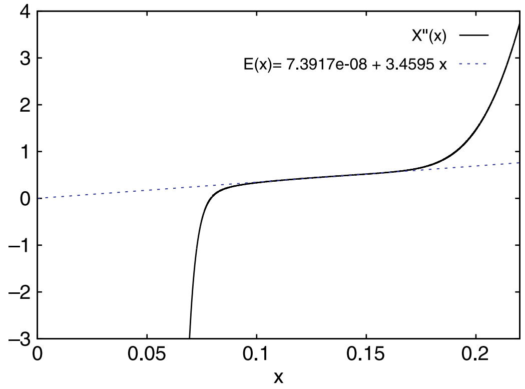

Fig. 12. Extrapolation of $X''_{500}(x)$ for the annulus.

5.2.2. Annulus

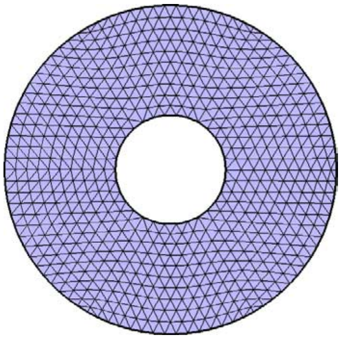

Using the Laplace–Beltrami operator on a parametrization of the annulus with outer radius 1 and inner radius 1/3 for the computation of the spectrum, we extracted its area and boundary length exactly at least up to the third decimal place and obtained the number of holes $h=1$ (since c_2 is almost zero, as can be seen in Fig. 12).

5.2.3. Sphere

The sphere with radius 1 has a surface area of $4\pi\approx 12.5664$. We extracted the area

$$A = 12.557 \tag{46}$$

from the computed eigenvalues employing the Laplace–Beltrami operator on the surface. The boundary length $L=0$ is already known from the fact that the first eigenvalue is also zero (since the sphere is a closed surface, cf. Section 2.1). The extracted Euler characteristic

$$E = 1.902 \approx 2 \tag{47}$$

is a close approximation to the real characteristic. The results can be found in Table 2.

Table 2
Geometric data of sphere

	Real	Extracted	Error (%)
A	12.5664	12.557	0.075
E	2	1.902	–

Table 3
Geometric data of ellipsoidal hemisphere

	Real	Extracted	Error (%)
A	8.459	8.459	0
L	$2\pi \approx 6.283$	6.25761	0.404

5.2.4. Ellipsoidal hemisphere

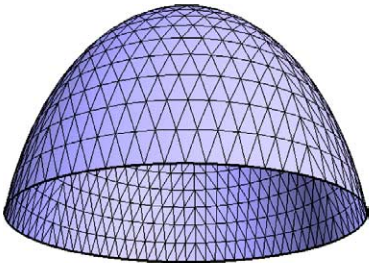

The ellipsoidal hemisphere with radii ($r_1 = r_2 = 1$, $r_3 = 1.5$) serves as an example for a bounded, curved surface. The extracted surface area and boundary length together with the relative error can be found in Table 3.

5.2.5. Ball

For the solid ball we deformed a cube using the parametrization as described in Section 6.1. Even the extraction of the volume V and the boundary surface area A for this smoothly bounded 3d solid was possible. Table 4 presents the exact and the extracted values together with the relative error. We notice a larger error than in the 2d surface examples presented above. This is due to the fact that the additional complexity of the new dimension results in denser and larger matrices and therefore allows only coarser meshes. As we will show later, these coarse meshes are good enough for the first lowest eigenvalues to be quite accurate. The larger λ_n with n around 500 however show errors up to 11%. We also obtained similar results for the unity cube (see [55]).

5.2.6. Remarks

Furthermore, we obtained very good results for the torus extracting its area and Euler characteristic (see [55]), employing the ‘Atlas’ data structure for the construction and computation. In all examples above we used only the first 500 eigenvalues. Of course all of the shown values can be improved if higher sufficiently correct eigenvalues are used (using a higher refinement of the mesh or more accurate and faster computation methods available for special cases, e.g. planar shapes).

Table 4
Geometric data of the ball

	Real	Extracted	Error (%)
V	$4/3\pi r^3 = 4.18879$	$c_0 = 4.058$	3.12
A	$4\pi r^2 = 12.56637$	$(-2/\sqrt{\pi})c_1 = 12.049$	4.12

6. Applications

Before we look at some application examples, we want to give a brief overview on the necessary steps described so far:

(1) *Pre-process.* Some objects might need to be pre-processed for the computation of the eigenvalues. Pre-processing includes, e.g. conversion into a dataformat supported by the FEM engine (like triangular meshes, surface parametrizations such as spline patches or composed patches as a ‘structural atlas’, tetrahedrizations of solids, parametrized solids). If the given object is not a manifold, or consists of several separated components, it first has to be repaired or the desired component has to be selected. If the eigenvalue computation of a scene containing several components is carried out at once the resulting Shape-DNA is the union of the eigenvalues of the single components ordered by size. In such a case, shape matching is still possible (if, e.g. the whole scene needs to be compared to a scene with similar components or if single components shall be found) whereas the extraction of geometric data cannot be accomplished in this way.

(2) *Eigenvalue computation.* The computation of the eigenvalues is the most time consuming step. It can be done with the FEM method. In the case of a solid tetrahedrization or planar triangulation, a commercial software package can be employed for this task. For the parametrized objects (using the Laplace–Beltrami operator, Eq. (4)) and for 3d-meshes such a software package needs to be expanded, or proprietary FEM software solving the Helmholtz equation (6) for these cases needs to be developed. To get accurate results, remeshing or mesh refinement of the object might be necessary (see also Section 4). In some cases (where the initial mesh is too fine), mesh simplification can be applied to speed up the computation. The FE-method can be divided into two parts. The first part creates a discrete generalized eigenvalue problem $Ax = \lambda Bx$ with two large and sparse symmetric positive (semi-)definite matrices A and B (Eq. (34)). The second part solves this problem (employing standard libraries as, e.g. ARPACK or NAG). The computation time of the FE-method depends on the degrees of freedom (dimension of the matrices). The dimension depends on the number of elements (triangles or tetrahedra), on the connectivity of the mesh and on the degree used for the FEM computation. Usually, we use cubic elements. If the given surface or solid has a boundary, generally the Dirichlet boundary condition (fixed membrane) is applied. If objects with small holes or missing triangles are to be compared the Neumann boundary condition can be used instead, because the unwanted holes appear not to change the Neumann spectrum not as much as in the Dirichlet case.

(3) *Post-process.* When the eigenvalues of the surface or solid have been computed, they can be post-processed depending on the desired application. As will be described in the next sections, scaling can be undone using different approaches. Furthermore, geometric data can be extracted,

or the Shape-DNAs (vectors of eigenvalues) can be compared for shape identification or matching.

With the help of this Shape-DNA, several applications can be realized. As mentioned before, one can use the Shape-DNA to identify objects for the purpose of copyright protection, even when they are given in different representations. Similar objects having similar Shape-DNA can be detected fast by comparing only the Shape-DNA, enabling the use of our technique for database retrieval and shape matching. Furthermore, the Shape-DNA can be used for quality assessment, e.g. when converting or producing objects to prove that the shape of the converted object has not been modified. In order to apply our technique in these areas, three requirements need to be fulfilled:

- Firstly, the Shape-DNA needs to be very accurate, ensuring that the same Shape-DNA is calculated for an object when using different meshes or even when it is calculated analytically. This requirement can be fulfilled by using sufficiently dense meshes, since the convergence of the FEM is known.
- Secondly, similar but different objects should have different Shape-DNA, making it possible to discriminate between these objects. This property is only violated by the artificially constructed isospectral but not isometric objects (identical twins) described earlier. Anyhow, we will present evidence in Section 6.3.4 that for some isospectral 3d-solids, the Shape-DNA of the boundary surface can be used as a discrimination criterion.
- Thirdly, similar objects need to have similar Shape-DNA in order to detect the similarity. This requirement is completely fulfilled by the spectra. We will show in Section 6.3.6 that this property allows the detection of small deformation and leads to a clustering of similar objects when applied for shape matching.

In order to discriminate and compare similar objects via their Shape-DNA, a distance measure for Shape-DNA will be constructed. Before we look at the accuracy of the computation, we want to give Definition 3.

Definition 3 (*Shape-DNA*)
Let M be a Riemannian manifold with a metric g and let

$$\operatorname{spec}(M,g)=\{\lambda_0\leq\lambda_1\leq\lambda_2\leq\cdots\} \tag{48}$$

be the function computing the spectrum of (M, g) for a given boundary condition (we use the zero Dirichlet condition if not noted otherwise). $\operatorname{spec}:\mathcal{M}\to\mathbb{R}^{\mathbb{N}}_{\geq 0}$ maps a Riemannian manifold $(M,g)\in\mathcal{M}$ to the positive infinite dimensional space. The cropped spectrum containing only the first n eigenvalues

$$\operatorname{cspec}_n(M,g)=\{\lambda_0\leq\lambda_1\leq\lambda_2\leq\cdots\leq\lambda_n\}\in\mathbb{R}^n_{\geq 0} \tag{49}$$

is called Shape-DNA of (M, g) and can be seen as a point in the n-dimensional positive Euclidean space $\mathbb{R}^n_{\geq 0}$.

We compute these cropped spectra (Shape-DNA) containing a finite number n of eigenvalues (50–100, or up to 500 for the extraction of data), since the numerical computation of the whole spectrum is generally not possible.

6.1. Accuracy

At first we want to corroborate the requirement 'accuracy' by looking at a few example calculations where the exact eigenvalues are known. If not noted otherwise, the computation was done on a standard PC (AthlonXP running at 1667 MHz). The eigenvalues of the unit disk, for example, are the squares of the roots of the Bessel functions J_n [20, p. 261]. By approximating the area of the disk with linearly bounded triangles, one always gets a discretization error at the boundary. Therefore, the resulting eigenvalues are not very accurate compared to the superior technique used below. In this computation (with cubic elements and 4021 degrees of freedom), the first eigenvalue already shows an error of approx. 0.067%. Higher eigenvalues are even more erroneous. These results can be improved by exploiting the fact that the Laplace–Beltrami operator (due to its invariance properties) yields the same eigenvalues even if a different parametrization of the same surface is applied. Of course, the Laplace–Beltrami operator can be applied to parametrizations of planar objects as well as for surfaces in 3d. In this example, we choose a special parametrization f (not the identity as above) defined on a polygonal parameter space glued to itself at the appropriate boundary edges (as can be seen in Fig. 13). This parametrization f maps the triangular parameter space onto the disk

$$f(u,v)=rv\begin{pmatrix}\cos\dfrac{\pi u}{v}\\ \sin\dfrac{\pi u}{v}\\ 0\end{pmatrix}\quad\text{with } 0<v\leq 1,\ |u|\leq v \tag{50}$$

additionally defining $f(0, 0):=(0, 0, 0)$.

This method leads to a computation of the smoothly bounded disk without any discretization error at the boundary. Another advantage of the parametrization f (compared to polar coordinates, where a whole edge of the parameter space boundary collapses if $r=0$) is that we have well-behaved triangles at the center that do not degenerate when using a higher resolution (refinement). Therefore, with only 3781 degrees of freedom the first eigenvalue is exact up to the eighth decimal place and even λ_{99} is approximated with a relative error of only 0.027%.

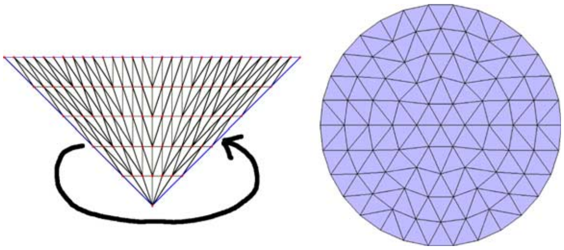

Fig. 13. Parameter space of the disk.

The aforementioned free choice of a parametrization that is especially suited for the numerical computation is only possible because of the property of the Laplace–Beltrami operator to be independent of any isometric reparametrization. This does not hold for the classical continuous Laplace operator since it operates on functions defined directly on the Euclidean space (with Euclidean metric). Generally, we observe an advantage of the Laplace–Beltrami operator over the simple Laplacian even for planar domains: using the free choice of a parametrization we have utilized something like 'free form finite elements'. That way, any surface can be triangulated without discretization error at the boundary. The computations of eigenvalues based on these parametrizations are very accurate.

Remark 1 (*Spectral determination of some shapes*)
Since we know what happens to the eigenvalues when scaling the area (see Section 2), the eigenvalues of a disk with radius r can be calculated as

$$\lambda_{n,m} = \frac{k_{n,m}^2}{r^2} \text{with the Bessel function } J_n(k_{n,m}) = 0 \tag{51}$$

Kac [40] proved that no planar shape is isospectral to the disk, except the disk itself. Therefore, given a planar shape, it is possible to calculate the radius with the first eigenvalue

$$r \approx \frac{k_{0,1}}{\sqrt{\lambda_1}} \tag{52}$$

It is then possible to test the assumption that a given shape is a disk with further eigenvalues. In fact, all Euclidean balls are determined among solids by their spectra in any dimension. This follows from the fact that the volume and the boundary area of the domain are determined by its spectrum (cf. heat coefficients in Eq. (18)) and using that an isoperimetric region (a region with maximal volume related to the boundary size) in $\mathbb{R}^n$ is always a ball (see [3]). A similar argument leads to the result that all regular polygons $D \in \mathbb{R}^2$ with n sides are spectrally determined among planar polygons with not more than n sides (since the area and boundary ratio is again fixed by an isoperimetric equality [3]). Furthermore, Tanno [59] proved that all round spheres in dimensions up to 6 are completely characterized by their spectra. For higher dimensions, the validity of this result appears to be still open.

A similar eigenvalue calculation as in the disk case can be done for the sphere. Even though the sphere is a surface with curvature, the eigenvalues computed with this parametrization are very accurate. With 5447 nodal points we approximated

$$\lambda_{101} = 110 \approx 110.55599 \tag{53}$$

with a relative error of 0.5055% in 4 s and with 11,522 nodal points we obtained

$$\lambda_{101} = 110 \approx 110.0003989 \tag{54}$$

with a relative error of only 0.0004% in 73 s. Generally, these high resolutions are not necessary for most applications.

In order to show that we can use a 3d triangle mesh (a surface consisting of planar triangular faces) instead of a parametrized surface as input, we calculated the eigenvalues of a triangle mesh approximating the unit sphere with 11,522 degrees of freedom and 2560 triangles using cubic elements in 5 s. The eigenvalues

$$\lambda_1 \approx 0, \quad \lambda_{24} \approx 2.005, \quad \lambda_{45} \approx 6.014\ldots \tag{55}$$

are very close to the eigenvalues of the sphere (0, 2 and 6), as expected, since the triangle mesh approximates the real surface very exactly (with a maximal distance of only 0.0026) and because of the continuity property of the spectrum (cf. Section 2.1). Yet it should be noted that this faceted sphere is of course only an approximation and not the sphere itself, therefore the spectra have to differ slightly from each other. An advantage of using polygonal meshes instead of parametrized surfaces is that no numeric integration (cubature) is needed by the FE-method for the construction of the matrices. Since all triangles are planar, the integral equations (34) can be evaluated for the unity triangle once and then transported to an arbitrary triangle, resulting in an enormous speed-up in computation.

For the computation of the eigenvalues of the round sphere, the parameter space of the sphere was glued to itself. Similarly, we computed the eigenvalues of tori. Since the correct eigenvalues of non-flat tori are not known from theory, they cannot be used to verify our computations and will therefore not be discussed here. More complex objects can be constructed by gluing different patches to each other. The cylinder with spherical caps presented in Section 4 and Fig. 5, for example, consists of three surface patches. Since the real eigenvalues of this compound surface can be derived from results in [4], we will present a comparison with our values (see Table 5). For the first computation, we used the Laplace–Beltrami operator on the surface with 4056 cubic elements (18,254 degrees of freedom) to approximate the eigenvalues very exactly. The construction of the matrices A and B together with the pre-processing (refinement) took 58 s and the computation of the first 10 smallest eigenvalues using the ARPACK library approx. 5 s. In a faster computation, we only used 216 cubic elements (974 degrees of freedom) and computed the shown values in 3 s.

As examples of 3d-solids we will look at the 3d-cube and the 3d-ball. The eigenvalues of the cuboid with side lengths a, b, c are known from theory

$$\lambda_{M,N,O}^{\Omega} = \pi^2\left(\frac{M^2}{a^2} + \frac{N^2}{b^2} + \frac{O^2}{c^2}\right) \text{ with } M,N,O = 1,2,\ldots \tag{56}$$

Table 5
Eigenvalues of the cylinder with spherical caps

EV	Real	FEM (18,254)	FEM (974)
Time	–	58 s+5 s	3 s+0 s
λ_1	0	0	0
λ_2	0.5974034	0.5974034	0.5974034
λ_3, λ_4	1.3450307	1.3450624	1.3456242
λ_5	2.1930427	2.1930427	2.1930430
λ_6, λ_7	2.5588079	2.5589283	2.5610538
λ_8	4.4586760	4.4586760	4.4586826
λ_9	4.5416743	4.5416754	4.5421094

The eigenvalues can also be computed numerically, using the Laplacian in Euclidean space, a tetrahedrization of the cube and an appropriate FEM computation. The smallest computed eigenvalues are close to the correct ones:

$$\begin{aligned}\lambda_{1,1,1} &= 29.6112 \approx 29.6088,\\ \lambda_{2,1,1} &= 59.2343 \approx 59.2176\end{aligned} \tag{57}$$

This computation was done with 6144 quadratic elements (tetrahedra) resulting in 7471 degrees of freedom. The construction of the matrices took 18 s and the computation of the first 10 eigenvalues 20 s.

In the case of the ball, the computation is even more interesting, since it is smoothly bounded and cannot be discretized with linearly bounded tetrahedra without error. Therefore, we used a tetrahedrized cube as parameter space and the 3d-Laplace–Beltrami operator to calculate the eigenvalues of the ball (see Fig. 14 for the tetrahedrization). Our parametrization (with $\|\cdot\|_\infty$, $\|\cdot\|_2$ being the maximum and Euclidean norm, respectively)

$$f(u,v,w) = \frac{\|(u,v,w)\|_\infty}{\|(u,v,w)\|_2}\begin{pmatrix}u\\v\\w\end{pmatrix} \tag{58}$$

shrinks the cube with $-1 \le u,\ v,\ w \le 1$ onto the unit ball, mapping the boundary of the cube onto the boundary of the ball, thus making it possible to carry out the calculation without having to glue the solid to itself but still without discretization error at the boundary. The first approximated eigenvalues, using the same resolution as in the example above

$$\begin{aligned}\lambda_1 &= 9.88 \approx 9.8696,\\ \lambda_2 &= 20.357 \approx 20.1907\end{aligned} \tag{59}$$

are close to the real values (known from theory) but higher eigenvalues are getting inaccurate due to the calculation with a low resolution (refinement). In this example, the computation of the matrices took 155 s and the computation of the first 10 eigenvalues 47 s.

6.2. Distance of Shape-DNAs

For the purpose of shape comparison and identification, we need to apply a distance calculation to the spectra. In most cases shape comparison is applied to objects independent of their size. Therefore, the Shape-DNAs (spectra) need to be normalized first. Such a normalization can be achieved by scaling the vector containing the eigenvalues with an appropriate scaling factor. The following normalization methods are possible: The Shape-DNA of a d-dimensional Riemannian manifold can be…

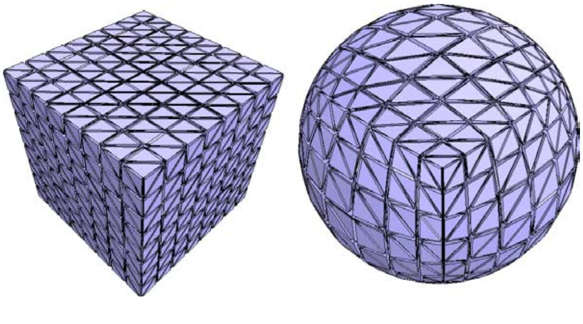

Fig. 14. Ball with parameter-cube.

(1) …divided by its first non-zero eigenvalue.
(2) …divided by the factor c of the fitting curve

$$f(x) = cx^{2/d} \tag{60}$$

fitting $f(n) := \lambda_n$ (cf. Weyl's law in Eqs. (9) and (10)). For $d=2$ the factor c is simply the slope of the fitting line. The dimension d can easily be determined if enough eigenvalues are given.
(3) …multiplied by $V^{2/d}$, where V is the Riemannian volume of the manifold extracted by extrapolation from the spectrum (for $d=2$ this is simply a multiplication by the surface area).
(4) …multiplied by $V^{2/d}$, where V is the real Riemannian volume that has been calculated externally via a preprocess (again for $d=2$ this is simply a multiplication by the surface area).
(5) …multiplied by s^2, if the scaling factor s of a given object is known.

The first normalization method is sufficient when trying to identify an object, since the Shape-DNA will be exactly the same after normalization. The methods two to four can be used if similar shapes are to be detected. It should be noted that the slope of the fitting line is a rough approximation to $4\pi/A$, where A is the area of the two-dimensional manifold (see 'Weyl's Law' equation (9) in Section 2.3).

In the next step, the normalized Shape-DNAs are cropped to lower the number of eigenvalues n (to 10–100) and the mutual Euclidean distances of the resulting n-dimensional vectors of eigenvalues can be calculated. Let $\Lambda = (\lambda_1, \lambda_2, \ldots, \lambda_n)$ and $M = (\mu_1, \mu_2, \ldots, \mu_n)$ two n-dimensional Shape-DNAs then the p-norm of the distance can be expressed as

$$d_{p,n}(\Lambda, M) := \|\Lambda - M\|_{p,n} = \left(\sum_{i=1}^{n} (\lambda_i - \mu_i)^p\right)^{1/p} \tag{61}$$

The Euclidean distance is simply $d_{2,n}$. It is possible to use a different distance (another p-norm, a symmetric Hausdorff distance or the correlation) but our results show that the Euclidean distance leads to good results. Further research will be done on applying different weights to the eigenvalues (for example, emphasizing the smaller eigenvalues by dividing λ_n through n).

6.3. Examples

6.3.1. Independence of representation

For the application of copyright protection, database retrieval and quality assessment it is necessary that shapes can be identified, even if the object has a different parametrization, with a different spatial position and size. Therefore, we computed the Shape-DNAs of the three B-Spline patches B1, B1′ and B2 (backs of display dummies) that can be found in Appendix. The patch B1′ is a scaled, translated and rotated version of patch B1 where the degree has been additionally raised. Patch B2 is a deformation of B1 with a leaner waist and smaller shoulders. As expected, the Shape-DNA of B1 and B1′ are almost identical (distance $d_{2,50}=0.079$) while the one of B2 differs from the others by a distance of $d_{2,50}=45.6$ (when scaling with the fitting line and using $n=50$ values). When using different meshes for the calculation, a different representation as a height function or even when introducing small errors (at the control points), the Shape-DNA comparison leads to the same clear results.

6.3.2. Continuous dependence on shape

In the subsequent example, we deform an ellipsoid and plot the first eigenvalues. The deformation starts with an ellipsoid with radius 1 in x and y direction and 0.5 in z direction. Then the z-radius was slowly shifted up to 1.5 in 100 steps. Fig. 15 shows that the eigenvalues move continuously, as discussed earlier and described in property [SIMILARITY]. In the case of the sphere (z-radius = 1 in step 50), the graphs describing the eigenvalues intersect because many eigenspaces coincide.

6.3.3. Discrimination power

To show how the spectrum can distinguish between different shapes with the same area, perimeter, incircle, circumcircle and sum of angles, the eigenvalues of the two polygons Isovol I1 and I2 (see Appendix) have been calculated. It can be seen in Table 6 that the first few eigenvalues of the two patches are quite different from each other. The Euclidean distance of the two normalized 50-dimensional Shape-DNAs is $d_{2,50}=53.5$. Even when transforming I1 slowly into I2 by moving the north bay to the right (and keeping the geometric properties specified above constant), the corresponding continuous movement of the eigenvalues can be detected.

Table 6
Eigenvalues of the iso-domains

EV	Patch 1	Patch 2	Diff.
λ_1	1.4303697	1.3619184	0.0684513
λ_2	2.9252157	2.4698985	0.4553171
λ_3	3.4078884	3.4220482	0.0141597
λ_4	4.0994027	3.8857960	0.2136067
λ_5	4.6141383	5.3698187	0.7556803

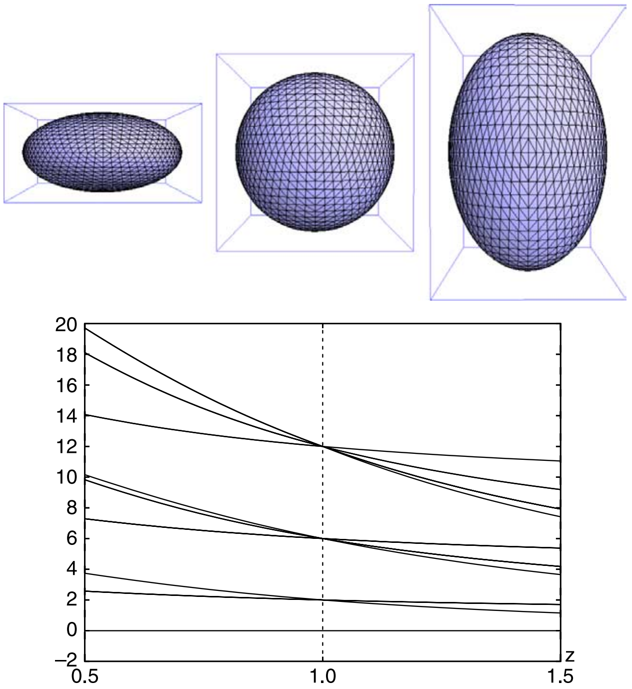

Fig. 15. Spectra of the ellipsoid deformation depends continuously on the shape.

6.3.4. Discrimination of the GWW-prisms

In Section 2.2, we presented an example of isospectral but not isometric planar shapes. Of course, isospectral but not congruent solid bodies in 3d as well. In fact they can be easily constructed from planar shapes by sweeping the isospectral 2d-domains into a third orthogonal direction for a distance h. The 3d prisms constructed that way are isospectral when they have the same height h. Fig. 16 shows two such prisms that were constructed with the planar GWW drums found by Gordon et al. [34]. The theoretical eigenvalues λ and the eigenfunctions f of the GWW-prisms with height h can be computed from the eigenvalues μ and the eigenfunctions s of the 2d-GWW-drums via this formula (for any constant c)

$$\lambda=\mu+l^2 \tag{62}$$

$$f(x,y,z)=s(x,y)c\sin(lz) \tag{63}$$

with $l:=(N\pi/h)$ and $N\in\mathbb{N}_{>0}$. This result can be obtained by separation of the new variable z in the Helmholtz equation (6). It can be verified quite easily by plugging the solution into (6) and noting that $\Delta s=-\mu s$ (since it was a solution to the 2d problem):

$$\Delta f=\Delta(cs\sin(lz)) \tag{64}$$

$$\Delta f=c(\Delta s\sin(lz)-sl^2\sin(lz)) \tag{65}$$

$$\Delta f=-(\mu+l^2)cs\sin(lz)=-(\mu+l^2)f \tag{66}$$

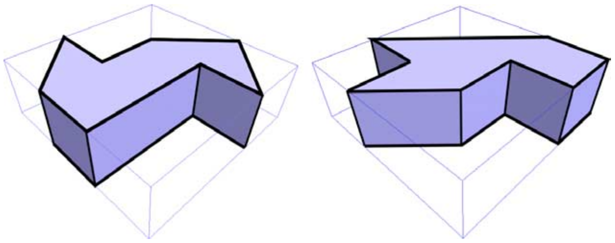

Fig. 16. GWW solid isospectral prisms.

Table 7
Eigenvalues of the GWW-prisms

EV	Theoretical	Prism 1	Prism 2
λ_1	5.0053451	5.0128509	5.0129320
λ_2	6.1229108	6.1317422	6.1317167
λ_3	7.6429605	7.6596645	7.6595216
λ_4	9.0049585	9.0151974	9.0153987

and by verifying the boundary condition for $z=0$ and h $(\sin(0)=0=\sin(lh))$.

At first we will present our computational results together with the theoretical results employing the eigenvalues of the planar GWW drums as computed very exactly by Driscoll [26]. It can be seen in Table 7 that eigenvalues of the two prisms (with height $h=2$) are very similar (due to their similar tetrahedrization). The computed eigenvalues are very close to the theoretical ones, even though this is a 3d example and the FEM computation in 3d is not as exact as in 2d because of the lower resolution possible.

The interesting fact about these 3d isospectral solids is that, even though they cannot be distinguished by the Shape-DNA of their body, the Shape-DNAs of their boundary shells can tell them apart. Since we can use a much higher mesh refinement in 2d, the computation of the shell will be much more accurate and reliable. In Table 8, we present the fourth eigenvalue of the two prism shells (with height $h=2$) for different mesh resolutions (edge length l).

It can be clearly seen that the difference is quite large (with 13%) and even grows when the refinement gets smaller and thus the computation more accurate. The computation with the highest resolution containing 3872 cubic elements and 17,426 degrees of freedom should be highly accurate. Still the construction of the matrices A and B took only a second, because all the faces are planar and therefore no numerical integration is needed. For triangle meshes in general, the integrals can be computed once for the unity triangle and then be transformed to an arbitrary triangle. The computation of the first 10 eigenvalues, on the other hand, took 928 s due to the high degree of freedom. Note that the computation in the case of the lowest resolution only takes 2 s and still yields sufficiently accurate results. There is even more evidence indicating that the Shape-DNA of the prism-shells has been computed sufficiently exact to distinguish the two shapes. We computed the eigenvalues of the shells scaled by $1.0/\sqrt{A}$, whose surface areas are equal to 1. Their resulting fourth eigenvalues are 39.4 and 45.3, respectively (of course still a difference of approx. 13%). Even though some eigenvalues differ that much, we were able to extract the area (1.004 and 1.007 for the two shells) very exactly by extrapolation using the first 500 eigenvalues. It is remarkable that even though the spectra of the two shells differ significantly, their surface areas, identical for both shells, can be computed very exactly from the different spectra.

Table 8
λ_4 of the GWW prism-shells

Edge	Prism 1	Prism 2	Diff-abs	Diff-rel (%)
l	0.57145	0.65719	0.08575	13.0474
$2l/3$	0.57133	0.65711	0.08578	13.0543
$0.5l$	0.57128	0.65708	0.08580	13.0571
$0.4l$	0.57125	0.65706	0.08581	13.0590

6.3.5. Database retrieval

In order to see how the Shape-DNA can help to distinguish many different surfaces, we applied our technique to a database of 1000 randomly generated B-Spline surface patches (with 3×3 up to 6×6 control points and degrees ranging from 2 to 4). For these patches the first 1741 eigenvalues were calculated and stored with the shapes. By using the Euclidean distance $d_{2,11}$ of the normalized (divided by λ_1) 11-dimensional vectors of eigenvalues, each patch could be uniquely identified even with deliberately different (not optimal) meshes introducing distinct calculation errors. Still, these inaccurate eigenvalues yielded distances of less than 0.02 between the original and the modified patch. Furthermore, from all the 500,000 possible pairs of different patches only 300 had a distance of less than 0.3 to each other, none was closer than 0.15. This confirms our assumption that our method is sensitive enough to be used for identifying patches even with reduced capacities for calculation (since only the first 11 eigenvalues were used). The construction of the matrices A and B for a given patch took approximately 100 s (we used the SISL Spline Library) and the computation of the first 10 eigenvalues took less than a second as did the actual comparison of a computed Shape-DNA with all the Shape-DNA contained in the database. The relatively slow construction of the matrices is due to the fact that for the computation of the integrals (Eq. (34)) in the case of a curved surface patch the g^{jk} of the patch are needed. In the case of triangulated surface meshes, the computation is clearly much faster, since all triangles are planar and no numerical integration is necessary. Fig. 17 shows an accumulated plot of the first 200 eigenvalues after normalization with the first eigenvalue λ_1. In an earlier experiment, we tried the same techniques using a database of 1625 randomly generated

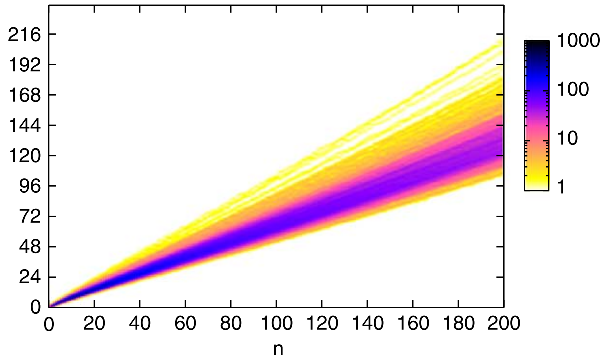

Fig. 17. Accumulated spectra (λ_n) of the patches.

polynomial patches of degree 10. The results were similar: Each patch could be easily identified by its first few eigenvalues.

It is perfectly possible that one could also identify any single NURBS patch within a large collection of NURBS patches using other isometric invariants like: boundary length, surface area, Gauss curvature integral, geodesic curvature of the boundary curve, Euler characteristic, etc. However, since these invariants contain very little information with respect to the amount of completeness up to which they determine the shape of an object, it is not very difficult to construct examples using (e.g. non-isometric) subdomains of the plane (see Section 6.3.3) and of the sphere sharing surface area, length and total curvature of their boundary curves. Those subdomains share also the Gauss curvature that is either zero or determined by the area of the respective domain in these examples. It confirms the discrimination power of the spectrum that those domains sharing the aforementioned geometric invariants have significant differences even in their respective first few eigenvalues (cf. Section 6.3.3). Obviously, the spectrum must have more discrimination power than the combination of the invariants consisting of length of boundary curves and surface area, as those invariants and even more information can be computed from the spectrum. Additionally, employing the spectrum of the double of the given surface, all the geometric information described in Section 2.3 can be obtained.

6.3.6. Shape matching

To demonstrate how the Shape-DNA can be used for shape matching we will calculate the Shape-DNAs of all the objects depicted in Appendix. We have already referred to B1, B1$'$, B2, I1 and I2 in Sections 6.3.1 and 6.3.3. The objects N1 and N2 (parts of a bottle neck) are deformations of each other (N2 is slimmer). The Shape-DNA of the unit square has been calculated with our FEM method (S1) and analytically. In the case of the square (even for an arbitrary rectangle, see Courant [20, p. 258]) the exact eigenvalues are known. Therefore, they can be used to verify the computational accuracy of our numerical results. The eigenvalues of a rectangular area with edge lengths a and b can be computed analytically as follows:

$$\lambda^{\Omega}_{M,N} = \pi^2\left(\frac{M^2}{a^2}+\frac{N^2}{b^2}\right) \quad \text{with } M,N=1,2,\ldots \tag{67}$$

For the comparison we also computed these exact values (represented by SR). The disk's Shape-DNA has been computed with a fine (D1) and a coarser (D2) mesh (both having smooth boundary) and by using a polygonal disk approximation (linearly bordered D3). All of these objects are now compared with each other in a way that not only identifies identical shapes, but also detects similarities. For this purpose, the Shape-DNAs were first normalized by the slope of the fitting line (Eq. (60)) and then cropped to contain only the first 50 eigenvalues. To visualize their positions, these vectors were embedded linearly into the two-dimensional space with the help of classical multidimensional scaling (MDS), a method performing a principal coordinate analysis (PCA). When plotting only the first two dimensions, the display error of the real mutual distances is kept as small as possible [21]. The 2d-MDS plot (Fig. 18) can be understood as an orthogonal projection of the 50-dimensional vectors onto their best 2d-fitting-plane. It shows very well how identical objects are mapped to the same spot and how similar objects form groups. These are very good results, considering that only the first two most important dimensions are plotted and that further information is contained in higher (less important) dimensions.

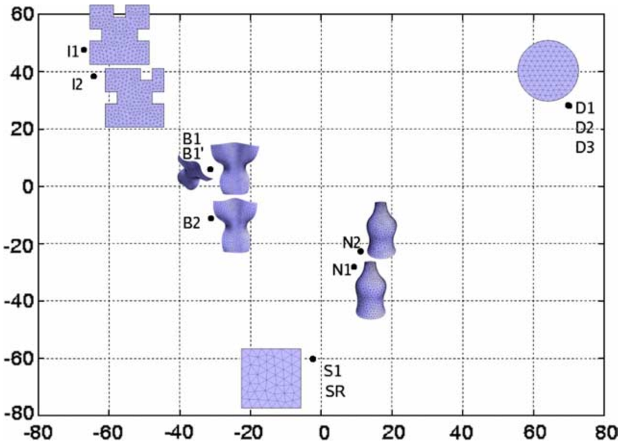

Fig. 18. 2d MDS plot of Shape-DNAs.

As a final example, we will compare the objects (given as triangular meshes) depicted in Appendix. The Shape-DNA of the rabbit has been computed for three meshes of different resolution (containing 10,000, 1000 and 400 triangles). The simplified meshes could be quickly obtained with the program QSlim (using a method described in Garland [31]). Since the rabbit looks like a deformed ellipsoid, we computed the Shape-DNA of the ellipsoid as well. The helmet is in fact nearly isometric to the ellipsoid, even though it does not look like it, because it consists of an inner and an outer shell, which are connected. Flipping the inner shell to the outside, one gets a deformed ellipsoid. Another group of test objects consists of animals (a camel, a cat, a cow and a horse), all of which have legs or arms, some have tails and some long necks. Another subject is the Santa, who is also equipped with arms and legs and wears a long jelly bag cap. The final test group is supplied by the screwdriver with its deformations. First the tip has been stretched and twisted, then bend over and last but not least the handle has been deformed. The stretching and the deformation of the handle are the most serious changes since the surface area (being a global feature) is modified.

The 2d MDS plot, that has been constructed like in the example before, can be seen in Fig. 19. Again we observe a nice clustering of the objects. The strongest modifications of the screwdriver are well reflected by the larger distance of the corresponding Shape-DNA projections. Furthermore, the deformed ellipsoids are well separated from the animals with the Santa. Note that the MDS plot is merely used for the visualization of the position of the 50-dimensional Shape-DNA. The measuring of the distance is done in higher dimensions. Even though the MDS plot shows the first two

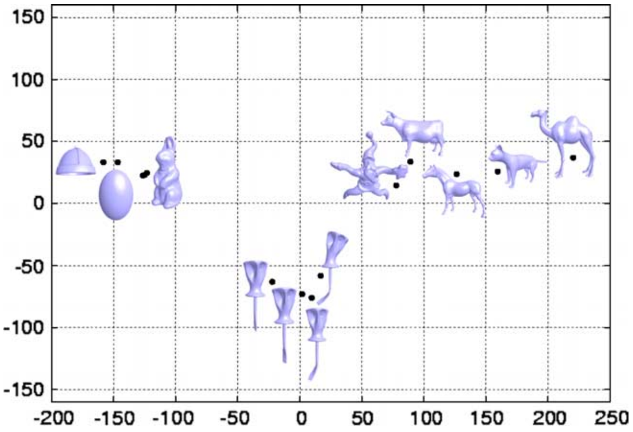

Fig. 19. 2d MDS plot of mesh Shape-DNAs.

most important principal components, important information might be contained in higher dimensions as well. A dimensionality reduction therefore might lead to the collapse of clusters onto each other. For real time database applications, the eigenvalues of an object have to be computed very fast. This can be achieved with coarser meshes (that can be constructed quickly) yielding very similar Shape-DNA as can be seen in the case of the rabbit.

Furthermore, when dealing with a large database, the search for nearest neighbors might be too slow in high dimensional spaces. Then it might be helpful that global shape information is already contained in the first eigenvalues while smaller details seem to be encoded in higher values. Because of the property [SIMILARITY], the Shape-DNA depends continuously on the shape deformation. As we have seen in Section 6.3.2, the deformation of an object changes the $\lambda_i(t)$ continuously with a deformation parameter t. Therefore, the Shape-DNA of all shapes that can possibly be obtained through a deformation of an object are contained in a path-connected subset.

It is generally possible that all n dimensions of the space containing the Shape-DNA are equally important when filled with the Shape-DNA of all deformations of a single shape. In real world applications we often want to compare one object with the finite amount of objects contained in a database. The Shape-DNA of these objects often do not vary equally strongly in all dimensions n. With the help of PCA we can choose the dimension $n_0 < n$ of the best fitting n_0-dimensional subspace (the shape space) in a way that keeps the approximation error of the set of Shape-DNA sufficiently small. This leads to a distinct dimensionality reduction with only little error. The Shape-DNA can then be represented in the lower dimensional shape space (in more than two dimensions as in the plots above, but still in less than the number of eigenvalues needed for efficient comparison). Similar to the approach of Turk and Pentland [61], who use eigenvectors of PCA (called eigenfaces) for face recognition, it can then be decided quickly if a new geometric object has a match in the database represented by the point set of Shape-DNA by measuring the distance of its Shape-DNA to shape space and by checking if its projection into shape space lies in or close to a cluster. If a Shape-DNA lies far away from the shape space and the corresponding object has to be added to the database, a new shape space has to be constructed, containing the new object. For this purpose, the PCA needs to be repeated for the Shape-DNA of all objects, so that future queries can again be processed quickly.

7. Conclusion

We have introduced a novel method that uses the eigenvalues of the Laplace–Beltrami operator as Shape-DNA (a fingerprint) for a given 2d or 3d manifold (surface or solid). Even though the proposed Shape-DNA does not meet the property [COMPLETENESS] entirely, since (artificially constructed) identical twins exist, we were able to demonstrate that it satisfies other important properties (like [ISOMETRY], [SCALING], [SIMILARITY], [EFFICIENCY], [COMPRESSION] and [PHYSICALITY]). We introduced the possibility of numerically calculating the Shape-DNA for different types of geometric objects (compound parametrized surfaces including NURBS, polygonal meshes and solid polyhedra). The computed results were shown to be independent of the given spatial location and scaled size and above all independent of the objects representation (especially of the chosen parametrization). Our method is also robust under variations in the quality of the model. We demonstrated that shape identification and comparison can be done using only a few eigenvalues, making it possible to locate objects rapidly within huge databases. Via comparison of the Shape-DNA, it is possible to compare a suspicious object with a copyrighted one to detect if the object might be an illegal copy. As shown, it is even possible to use the Euclidean distance of normalized Shape-DNA to detect similar objects. Shape-DNA can also be used as a quality measure when converting surfaces or solids into different representations utilizing the fact that the spectrum of a correctly converted object must agree with the spectrum of the original one.

We proved some propositions about the mutual independence of the eigenvalues and about the rapid convergence of the heat trace series. Moreover, we succeeded in numerically extracting the volume, boundary length and Euler characteristic from the computed Shape-DNA of the respective surface. Those numerical computations appear to be new.

Further research will extend this work to implicitly defined surfaces and solids employing, e.g. new concepts [12,50] useful to mesh implicit surfaces. As another extension, parallel processing and multigrid methods could be used to speed up and improve our eigenvalue computation making it possible to use higher resolutions and to compute spectra, especially of 3d-solids, more accurately. It is of interest as well as to study the combination of subdivision (or feature decomposition techniques) with the Shape-DNA to be able to match object parts. Additionally, more experiments will be done on larger shape databases (for meshes and for CAD-models), extending the concepts used for similarity detection (i.e. PCA) as described in the last section.

Appendix

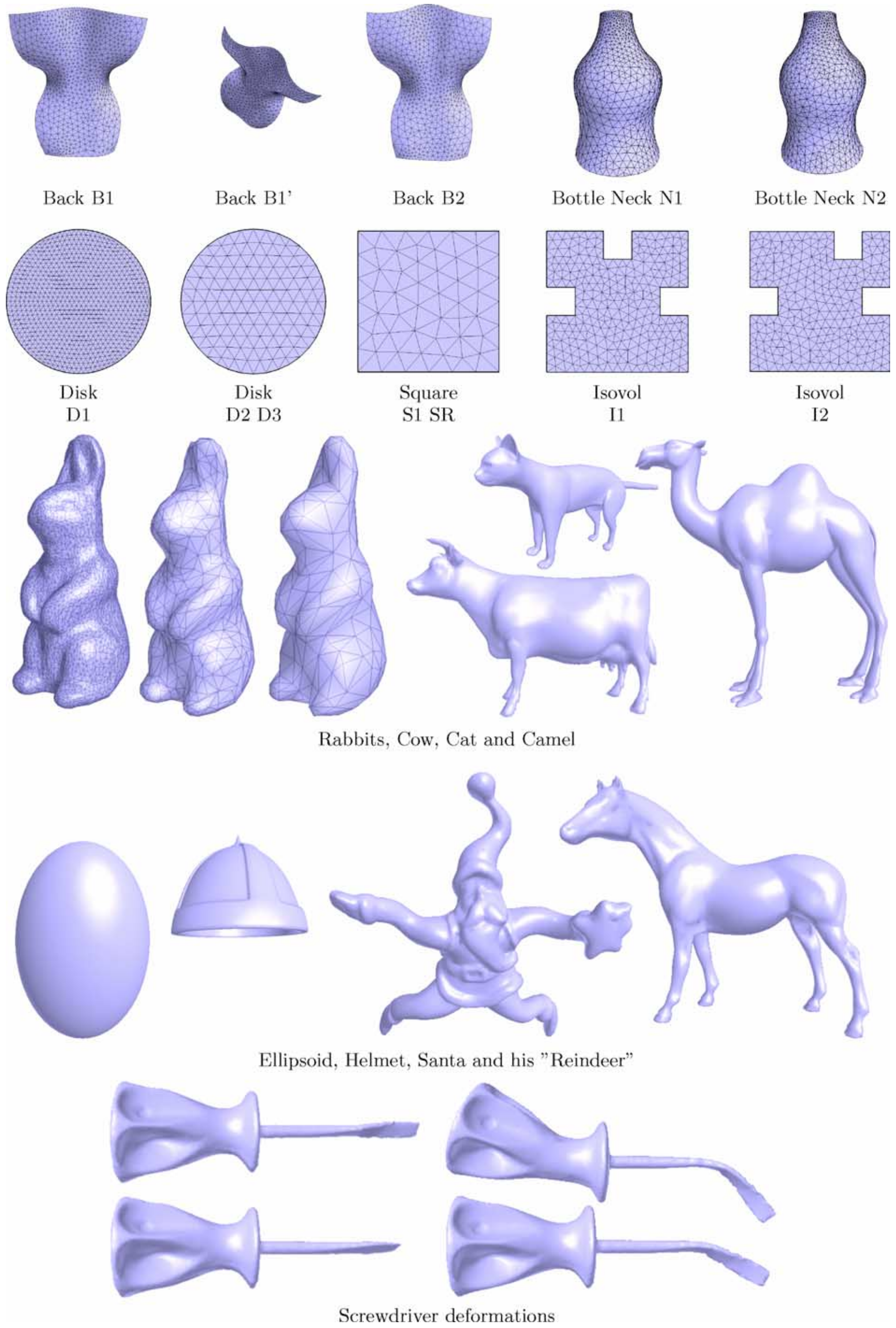

Back B1 Back B1' Back B2 Bottle Neck N1 Bottle Neck N2

Disk D1 Disk D2 D3 Square S1 SR Isovol I1 Isovol I2

Rabbits, Cow, Cat and Camel

Ellipsoid, Helmet, Santa and his "Reindeer"

Screwdriver deformations

References

[1] Adams C. The knot book. New York: Freeman; 1994.

[2] Ainsworth M, Oden J. A posteriori error estimation in finite element analysis. London: Wiley; 2000.

[3] Bandle C. Isoperimetric inequalities and applications. London: Pitman; 1980.

[4] Beekmann B. Eigenfunktionen und Eigenwerte des Laplaceoperators auf Drehflächen und die Gliederung des Spektrums nach den Darstellungen der Isometriengruppe. PhD Thesis. Mathematisches Institut der Universität Münster; 1988.

[5] Belkin M, Niyogi P. Laplacian eigenmaps for dimensionality reduction and data representation. Neural Comput 2003;15:1373–96.

[6] Benedens O. Geometry-based watermarking of 3D models. IEEE Comput Graphics Appl 1999;19(1):46–55.

[7] Berger M. Riemannian geometry during the second half of the 20th century. Providence, RI: American Mathematical Society; 2000.

[8] Berger M, Gauduchon P, Mazet E. Le spectre d'une variété riemannienne. Lecture notes in Mathematics, vol. 194. Berlin: Springer; 1971.

[9] Bespalov D, Shokoufandeh A, Regli WC, Sun W. Scale-space representation of 3d models and topological matching. In: ISM'03: Proceedings of the eighth ACM symposium on solid modeling and applications. New York: ACM Press; 2003. p. 208–15.

[10] Betcke T, Trefethen LN. Reviving the method of particular solutions. SIAM Rev 2005;47(3):469–91.

[11] Blascke W, Leichtweiβ K. Elementare differentialgeometrie. Berlin: Springer; 1973.

[12] Boissonnat J-D, Cohen-Steiner D, Vegter G. Isotopic implicit surface meshing. In: Proceedings of the 36th annual ACM symposium on theory of computing. New York: ACM Press; 2004. p. 301–9.

[13] Braess D. Finite elemente. Berlin: Springer; 1997.

[14] Bronstein AM, Bronstein MM, Kimmel R. Expression-invariant 3d face recognition. In: Proceedings of the AVBPA. Lecture notes in computer science no. 2688. Berlin: Springer; 2003. p. 62–9.

[15] Buser P. Geometry and spectra of compact Riemann surfaces. Basel: Birkhäuser; 1992.

[16] Buser P, Conway J, Doyle P, Semmler K-D. Some planar isospectral domains. Int Math Res Not 1994;9:391–400.

[17] Chavel I. Eigenvalues in Riemannian geometry. London: Academic Press; 1984.

[18] Chen H, Bishop J. Delaunay triangulation for curved surfaces. In: Sixth international meshing roundtable proceedings; 1997. p. 115–27.

[19] Colin de Verdière Y. Construction de Laplaciens dont une partie finie du spectre est donnée. Ann Sci Ecole Norm S 1987;20(4):599–615.

[20] Courant R, Hilbert D. Mehods of mathematical physics, vol. I. New York: Interscience; 1953.

[21] Cox TF, Cox MAA. Multidimensional scaling. 2nd ed. London: Chapman & Hall; 2001.

[22] Craioveanu M, Puta M, Rassias T. Old and new aspects in spectral geometry. Dordrecht: Kluwer; 2001.

[23] Cuthill E, McKee J. Reducing the bandwidth of sparse symmetric matrices. In: Proceedings of the 24th ACM national conference; 1969. p. 157–72.

[24] Descloux J, Tolley M. An accurate algorithm for computing the eigenvalues of a polygonal membrane. Comput Methods Appl Mech Eng 1983;39:37–53.

[25] do Carmo MP. Differential geometry of curves and surfaces. Englewood Cliffs, NJ: Prentice-Hall; 1976.

[26] Driscoll T. Eigenmodes of isospectral drums. SIAM 1997;39(1):1–17.

[27] Elad A, Kimmel R. On bending invariant signatures for surfaces. IEEE Trans PAMI 2003;25(10):1285–95.

[28] Feller W. An introduction to probability theory and its applications, vol. II. London: Wiley; 1971.

[29] Fox L, Henrici P, Moler C. Approximations and bounds for eigenvalues of elliptic operators. SIAM J Numer Anal 1967;4:89–102.

[30] Funkhouser T, Min P, Kazhdan M, Chen J, Halderman A, Dobkin D, et al. A search engine for 3d models. ACM Trans Graph 2003;22(1): 83–105.

[31] Garland M, Heckbert PS. Surface simplification using quadric error metrics. Comput Graphics Annu Conf Ser 1997;31:209–16.

[32] Gel'fand I. Automorphic functions and the theory of representations. In: Proceedings of the international congress of mathematics. Stockholm: Almqvist & Wiksell; 1963. p. 74–85.

[33] Gordon C, Webb D. Isospectral convex domains in euclidean space. Math Res Lett 1994;1:539–45.

[34] Gordon C, Webb D, Wolpert S. Isospectral plane domains and surfaces via Riemannian orbifolds. Invent Math 1992;110:1–22.

[35] Grimes RG, Lewis JG, Simon HD. A shifted block lanczos algorithm for solving sparse symmetric generalized eigenproblems. SIAM J Matrix Anal Appl 1994;15(1):228–72.

[36] Halbeisen L, Hungerbühler N. Reconstruction of weighted graphs by their spectrum. Eur J Comb 2000;21(5):641–50.

[37] Hilaga M, Yoshihisnagawa, Kohmura T, Kunii TL. Topology matching for fully automatic similarity estimation of 3d shapes. In: SIGGRAPH 2001. New York: ACM Press; 2001. p. 203–12.

[38] Huntebrinker W. Numerische Bestimmung von Eigenwerten des Laplace—Beltrami-Operators auf dreidimensionalen hyperbolischen Räumen mit Finite-Element-Methoden. PhD Thesis. Heinrich-Heine-Universität Düsseldorf; 1995.

[39] Iyer N, Jayanti S, Lou K, Kalyanaraman Y, Ramani K. Three-dimensional shape searching: state-of-the-art review and future trends. Comput Aided Des 2005;37(5):509–30.

[40] Kac M. Can one hear the shape of a drum? Am Math Mon 1966;73(4): 1–23.

[41] Karni Z, Gotsman C. Spectral compression of mesh geometry. In: Akeley K, editor. Siggraph 2000, computer graphics proceedings. New York: ACM Press; 2000. p. 279–86.

[42] Ko KH, Maekawa T, Patrikalakis NM, Masuda H, Wolter F-E. Shape intrinsic fingerprints for free-form object matching. In: Proceedings of the eigth ACM symposium on solid modeling and applications; June 2003. p. 196–207.

[43] Ko KH, Maekawa T, Patrikalakis NM, Masuda H, Wolter F-E. Shape intrinsic properties for free-form object matching. ASME J Comput Inf Sci Eng 2003;3(4):325–33.

[44] McKean H, Singer I. Curvature and the eigenvalues of the Laplacian. J Differ Geom 1967;1:43–69.

[45] Minakshisundaram S. Eigenfunctions on Riemanian manifolds. J Indian Math Soc 1953;17:159–65.

[46] Minakshisundaram S, Pleijel A. Some properties of the eigenfunctions of the Laplace-operator on Riemannian manifolds. Can J Math 1949;1: 242–56.

[47] Numerical-Algorithms-Group. NAG-FORTRAN library. http://www.nag.co.uk

[48] Ohbuchi R, Masuda H, Aono M. A shape-preserving data embedding algorithm for nurbs curves and surfaces. In: Proceedings of CGI'99. Silver Spring, MD: IEEE Computer Society; 1999. p. 180–7.

[49] Ohbuchi R, Mukaiyama A, Takahashi S. A frequency-domain approach to watermarking 3d shapes. Comput Graphics Forum 2002;21(3): 373–82.

[50] Ohtake Y, Belyaev AG. Dual/primal mesh optimization for polygonized implicit surfaces. In: Proceedings of the seventh ACM symposium on solid modeling and applications. New York: ACM Press; 2002. p. 171–8.

[51] Okabe A, Boots B, Sugihara K, Chiu SN, Sugihara K, Chiu SN. Spatial tessellations. London: Wiley; 1992.

[52] Osgood B, Phillips R, Sarnak P. Compact isospectral sets of surfaces. J Funct Anal 1988;80:212–34.

[53] Prokop RJ, Reeves AP. A survey of moment-based techniques for unoccluded object representation and recognition. CVGIP Graph Models Image Process 1992;54(5):438–60.

[54] Protter MH. Can one hear the shape of a drum? Revisited. SIAM Rev 1987;29(2):185–97.

[55] Reuter M. Laplace spectra for shape recognition. PhD Thesis. Divison of Computer Graphics, Institute for Man Machine Interaction, University of Hannover; 2005.

[56] Reuter M, Wolter F-E, Peinecke N. Laplace-spectra as fingerprints for shape matching. In: SPM'05: Proceedings of the 2005 ACM symposium on solid and physical modeling. New York: ACM Press; 2005. p. 101–6.

[57] Seifert H, Threlfall W. A textbook of topology. Pure and applied mathematics, vol. 89. London: Academic Press; 1980.

[58] Strang G. Introduction to applied mathematics. Reading, MA: Wesley—Cambridge Press; 1986.

[59] Tanno S. Eigenvalues of the Laplacian of Riemannian manifolds. Tôhoku Math J 1973;25:391–403.

[60] Tucker TM, Kurfess TR. Newton methods for parametric surface registration. Part I. Theory. Comput Aided Des 2003; 35(1):107–14.

[61] Turk M, Pentland A. Eigenfaces for recognition. J Cogn Neurosci 1991; 3(1):71–86.

[62] Weyl H. Über die asymptotische Verteilung der Eigenwerte. Nachrichten von der (königlichen) Gesellschaft der Wissenschaften zu Göttingen; 1911. p. 110–7.

[63] Weyl H. Das asymptotische verteilungsgesetz der eigenwerte linearer partieller differentialgleichungen. Math Ann 1912;441–69.

[64] Wolter F-E. Cut locus and medial axis in global shape interrogation and representation. MIT sea grant report MIT-T-93-002. US National Sea Grant Library; 1993. 44 pp.

[65] Wolter F-E, Friese K. Local and global geometric methods for analysis, interrogation, reconstruction, modification and design of shape. In: Proceedings of the CGI'00. Silver Spring, MD: IEEE Computer Society; 2000. p. 137–51.

[66] Wolter F-E, Peinecke M, Reuter N. Geometric modeling of complex shapes and engineering artifacts. In: Stein E, de Borst R, Hughes T, editors. Encyclopedia of computational mechanics, vol. 1. London: Wiley; 2004. p. 475–95 [chapter 16].

[67] Wolter F-E, Reuter M, Peinecke N. Verfahren zur Charakterisierung von Objekten, German patent application 10 2005 025 578.7, pending; 2005.

[68] Xu G. Discrete Laplace—Beltrami operators and their convergence. Comput Aided Geom Des 2004;21:767–84.

[69] Zelditch S. The inverse spectral problem for surfaces of revolution. J Differ Geom 1998;49(2):207–64.

[70] Zienkiewicz O, Taylor R. The finite element method—volume 1: the basis. London: Butterworth & Heinemann; 2000.

Martin Reuter obtained his Diploma (MSc) in mathematics with a second major in computer science and a minor in business information technology from the University of Hannover in 2001. He is a PhD student at the Welfenlab, Division of Computer Graphics at Hannover University and just completed his PhD thesis in the area of shape recognition. His research interests include computational geometry and topology, computer aided design, geometric modeling and computer graphics.

Dr. Wolter has been a full professor of computer science at the University of Hannover since the winter term of 1994/1995 where he directs the Division of Computer Graphics and Geometric Modeling called Welfenlab. Before coming to Hannover, Dr. Wolter held faculty positions at the University of Hamburg (in 1994), MIT (1989–1993) and Purdue University in the USA (1987–1989). Prior to this he developed industrial expertise as a software and development engineer with AEG in Germany (1986–1987). Dr. Wolter obtained his PhD in 1985 from the department of mathematics at the Technical University of Berlin, Germany, in the area of Riemannian manifolds. In 1980 he graduated in mathematics and theoretical physics from the Free University of Berlin. At MIT Dr. Wolter codeveloped the geometric modeling system Praxiteles for the US Navy from 1989 to 1993 and published various papers that broke new ground applying concepts from differential geometry and topology on problems and design of new methods used in geometric modeling and CAD systems. Dr Wolter is a research affiliate of the MIT department of mechanical engineering.

Niklas Peinecke received his Diploma (MSc) in mathematics with a second major in computer science and a minor in sociology in 2001 at the University of Hannover. Presently, he is a PhD student at the Welfenlab, Division of Computer Graphics. His research interests include image recognition, computational geometry and topology, computer graphics and object oriented programming theory.